# NON-EQUISPACED FOURIER NEURAL SOLVERS FOR PDES

**Haitao Lin, Lirong Wu, Yongjie Xu, Yufei Huang, Siyuan Li, Guojiang Zhao & Stan Z, Li**
AI Lab, Research Center for Industries of the Future, Westlake University
{linhaitao, stan.zq.li}@westlake.edu.cn

## ABSTRACT

Recently proposed neural resolution-invariant models, despite their effectiveness and efficiency, usually require equispaced spatial points of data for solving partial differential equations. However, sampling in spatial domain is sometimes inevitably non-equispaced in real-world systems, limiting their applicability. In this paper, we propose a Non-equispaced Fourier PDE Solver (NFS) with adaptive interpolation on resampled equispaced points and a variant of Fourier Neural Operators as its components. Experimental results on complex PDEs demonstrate its advantages in accuracy and efficiency. Compared with the spatially-equispaced benchmark methods, it achieves superior performance with $42.85\%$ improvements on MAE, and is able to handle non-equispaced data with a tiny loss of accuracy. Besides, NFS as a model with mesh invariant inference ability, can successfully model turbulent flows in non-equispaced scenarios, with a minor deviation of the error on unseen spatial points.

## 1 INTRODUCTION

Solving the partial differential equations (PDEs) holds the key to revealing the underlying mechanisms and forecasting the future evolution of the systems. Recently, data-driven neural PDE solvers revolutionize this field by providing fast and accurate solutions for PDEs. Unlike approaches designed to model one specific instance of PDE (E & Yu, 2017; Bar & Sochen, 2019; Smith et al., 2020; Pan & Duraisamy, 2020; Raissi et al., 2020), neural operators (Guo et al., 2016; Sirignano & Spiliopoulos, 2018; Bhatnagar et al., 2019; KHOO et al., 2020; Li et al., 2020b;d; Bhattacharya et al., 2021; Brandstetter et al., 2022; Lin et al., 2022) directly learn the mapping between infinite-dimensional spaces of functions. They remedy the mesh-dependent nature of the finite-dimensional operators by producing a single set of network parameters that may be used with different discretizations.

However, a problem still exist – discretization-invariant modeling for non-equispaced data. On one hand, classical vision models and graph spatio-temporal models are not discretization-invariant, while the infinite neural operator like FNO (Li et al., 2020c) is. On the other hand, despite computational efficiency, vision models including FNO are equispace-necessary, and limited to handling images as 2-d regular grids. Therefore, two properties should be available in neural PDE solvers: *(1)* discretization-invariance and *(2)* equispace-unnecessity, and recently proposed methods can be classified into four types according to the two properties, as shown in Fig. 1.

As discussed, although the equispace-necessary methods enjoy fast parallel computation and low prediction error, they lack the ability to handle the spatially non-equispaced data. For these reasons, we aim to design a mesh-invariant model (defined in Fig. 1) called Non-equispaced Fourier neural Solver (NFS) with comparably low cost of computation and high accuracy, by lending the powerful expressivity of FNO and vision models to efficiently solve the complex PDE systems.

## 2 BACKGROUND AND RELATED WORK

### 2.1 PROBLEM STATEMENT

Let $D \in \mathbb{R}^d$ be the bounded and open spatial domain where $n_s$-point discretization of the domain $D$ written as $\boldsymbol{X} = \{\boldsymbol{x}_i = (x_i^{(1)}, \ldots, x_i^{(d)}) : 1 \leq i \leq n_s\}$ are sampled. The observation of input function $a \in \mathcal{A}(D; \mathbb{R}^{d_a})$ and output $u \in \mathcal{U}(D; \mathbb{R}^{d_u})$ on the $n_s$ points are denoted by $\{a(\boldsymbol{x}_i), u(\boldsymbol{x}_i)\}_{i=1}^{n_s}$, where

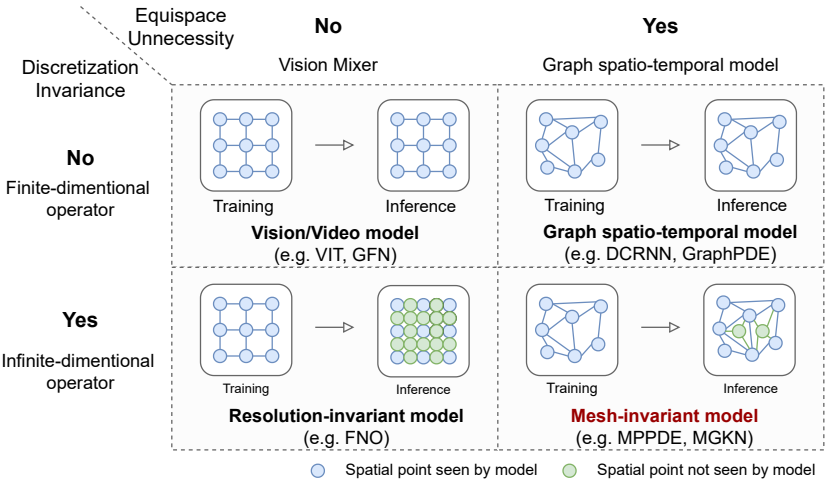


Figure 1: Four types of methods with or without the two concluded limitations.

$\mathcal{A}(D;\mathbb{R}^{d_a})$ and $\mathcal{U}(D;\mathbb{R}^{d_u})$ are separable Banach spaces of function taking values in $\mathbb{R}^{d_a}$ and $\mathbb{R}^{d_u}$ respectively. Suppose $\boldsymbol{x} \sim \mu$ is i.i.d. sampled from the probability measure $\mu$ supported on $D$. An infinite-dimensional neural operator $\mathcal{G}_\theta : \mathcal{A}(D;\mathbb{R}^{d_a}) \to \mathcal{U}(D;\mathbb{R}^{d_u})$ parameterized by $\theta \in \Theta$, aims to build an approximation so that $\mathcal{G}_\theta(a) \approx u$. To establish a mesh-invariant operator, $\boldsymbol{X}$ can be non-equispaced, and the learned $\mathcal{G}_\theta$ should be transferred to an arbitary discretization $\boldsymbol{X'} \in D$, where $\boldsymbol{x} \in \boldsymbol{X'}$ can be not necessarily contained in $\boldsymbol{X}$. Because we focus on spatially non-equispaced points, when the PDE system is time-dependent, we assume that timestamps $\{t_j\}$ are uniformly sampled.

### 2.2 Method Preliminaries

**Kernel integral operator method** (Li et al., 2020a) is a family of infinite-dimensional operators, in which $(\mathcal{G}_\theta(a))(\boldsymbol{x}) = Q \circ v^{\mathrm{T}} \circ \cdots \circ v^1 \circ P(a)(\boldsymbol{x})$ is formulated as an iterative architecture. A higher-dimensional representation function is first obtained by $v^0 = P(a) \in \mathcal{U}(D;\mathbb{R}^{d_v})$, where $P$ is a shallow fully-connected network. It is updated by

$$v^{\mathrm{t}+1}(\boldsymbol{x}) := \sigma(Wv^{\mathrm{t}}(\boldsymbol{x}) + \mathcal{K}_\phi(a)v^{\mathrm{t}}(\boldsymbol{x})), \qquad \forall \boldsymbol{x} \in D \tag{1}$$

where $\mathcal{K}_\phi : \mathcal{A} \to \mathcal{L}(\mathcal{U})$ is a kernel integral operator mapping, mapping $a$ to bounded linear operators, with parameters $\phi$. $W$ is a linear transform and $\sigma$ is a non-linear activation function. After the final iteration, $Q$ projects $v^{\mathrm{T}}(\boldsymbol{x})$ back to $\mathcal{U}(D;\mathbb{R}^{d_u})$.

**Fourier Neural Operator** (FNO) (Li et al., 2020d) as a member in kernel integral operator methodsLi et al. (2020a), updates the representation by applying the convolution theorem as:

$$\mathcal{K}_\phi(a)v(\boldsymbol{x}) = \mathcal{F}^{-1}(\mathcal{F}(\kappa_\phi) \cdot \mathcal{F}(v))(\boldsymbol{x}) = \mathcal{F}^{-1}(R_\phi \cdot \mathcal{F}(v))(\boldsymbol{x}), \tag{2}$$

The discrete Fourier transform of $f : D \to \mathbb{R}^{d_f}$ is denoted by $\mathcal{F}(f)(\boldsymbol{k}) \in \mathbb{C}^{d_f}$, with $\mathcal{F}^{-1}$ as its inverse. $R_\phi$ as the Fourier transform of a periodic kernel function $\kappa_\phi$, is directly learned as the parameters in the updating process. Because the sampled spatial points are equispaced in FNO, it can efficiently conduct fast Fourier transform (FFT) and its inverse (IFFT) to get the Fourier series.

**Vision Mixers** (Dosovitskiy et al., 2020; Tolstikhin et al., 2021; Rao et al., 2021; Guibas et al., 2021) are a line of models with a stack of (token mixing) - (channel mixing) - (token mixing) as their network structure for vision tasks. The defined tokens are equivalent to equispaced spatial points in the former definition. In specific, VIT uses a non-Mercer kernel function (Wright & Gonzalez, 2021) $\kappa_\phi$ to adaptively learn the pattern of message-passing through the iterative updating process

$$\begin{gathered} v^{\mathrm{t}+1}(\boldsymbol{x}) = \sigma(\mathrm{ChannelMix} \circ \mathrm{TokenMix}(v^{\mathrm{t}}(\boldsymbol{x}))); \\ \mathrm{TokenMix}(v(\boldsymbol{x})) = \sum_i \kappa_\phi(\boldsymbol{x},\boldsymbol{x}_i, v(\boldsymbol{x}), v(\boldsymbol{x}_i)) \cdot v(\boldsymbol{x}_i); \quad \mathrm{ChannelMix}(v(\boldsymbol{x})) = Wv(\boldsymbol{x}), \end{gathered} \tag{3}$$

where $W$ is a linear transform called channel mixing layer because it transforms the input on the channel of an image whose dimension is equivalent to function dimension $d_f$. We omit the residual connection in Eq. (1) for simplicity. Note that the FNO can be regarded as a member of the family

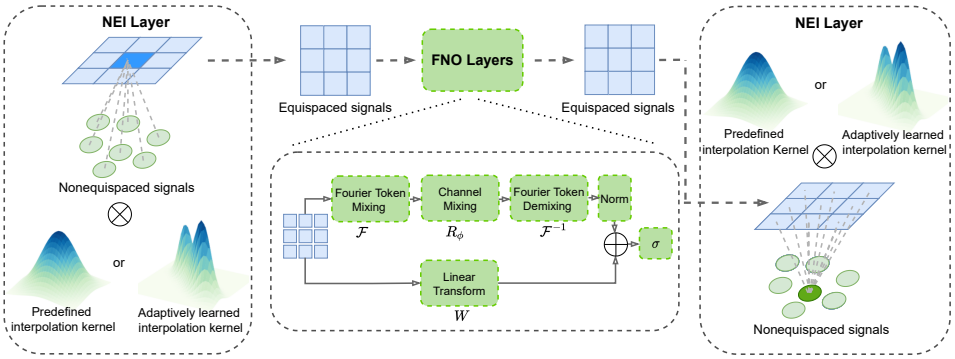


Figure 2: The architecture of NFS: In non-equispaced interpolation (NEI) layers, the kernels are adaptively learned rather than predefined, and the interpolated equispaced signals are processed through a stack of FNO layers with the same structure of Vision Mixers.

of Vision Mixers (See Appendix A). However, the powerful fitting ability and efficiency of Vision Mixers are limited to being applied to non-equispaced spatial points.

**Graph spatio-temporal models** (Seo et al., 2016; Li et al., 2018; Bai et al., 2020; Lin et al., 2021) as a solution to model non-equispaced spatial points, model interaction patterns among spatial points in a graph message-passing way, whose mechanism is similar to the token mixing in Vision Mixers. However, they suffer from high computational complexity and unsatisfactory accuracy.

## 3 Proposed Method

### 3.1 Non-equispaced Fourier Transform

Non-equispaced FFTs usually rely on a mixture of interpolation and the judicious use of FFT, where the calculations of interpolation are no more than $O(n_s \log n_s)$ operations (Kalamkar et al., 2012; Cheema et al., 2017). For example, Gaussian-based interpolation (Kestur et al., 2010) is commonly used. Denote $\mathcal{F}$ as equispaced FFT in particular, and $\mathcal{H}$ as the interpolation operator, and the proposed non-equispaced FFT is written as

$$(\mathcal{F} \circ \mathcal{H}(f))(\boldsymbol{k}) \approx \sqrt{\frac{\pi}{\tau}} e^{\tau <\boldsymbol{k},\boldsymbol{k}>} \sum_{j=1}^{m_s} e^{-2i\pi <\boldsymbol{k},\boldsymbol{x}_j>} \sum_{i=1}^{n_s} f(\boldsymbol{x}_i) h_\tau(\boldsymbol{x}_i - \boldsymbol{x}_j). \tag{4}$$

$\mathcal{H}(f)(\boldsymbol{x}_j) = \sum_{i=1}^{n_s} f(\boldsymbol{x}_i) h_\tau(\boldsymbol{x}_i - \boldsymbol{x}_j)$ interpolates values on resampled points via convolution with the periodic heat kernel $h_\tau(\boldsymbol{x} - \boldsymbol{y}) = \sum_{\boldsymbol{l} \in \mathbb{Z}^d} e^{-(\boldsymbol{x}-\boldsymbol{y})^2/4\tau}$, with $\tau$ as a constant.

### 3.2 Non-equispaced Fourier Neural PDE Solver

**Non-equispaced interpolation.** To harness the effectiveness of FNO, we use non-equispaced Fourier token mixing instead of the equispaced one. It generalizes the equispaced FFT in Eq. (2) as

$$\tilde{\mathcal{F}}(v) = (\mathcal{F} \circ \mathcal{H}_\eta(a))(v). \tag{5}$$

We denote $\mathcal{H}_\eta : \mathcal{A} \to \mathcal{L}(\mathcal{U})$ as the interpolation operator mapping, which maps parametric function to a bounded interpolation operator. $\mathcal{H}_\eta(a)$ gets the interpolated values on $m_s$ resampled equispaced points via the convolution with kernel $h_\eta$ as

$$(\mathcal{H}_\eta(a)v)(\boldsymbol{x}_j) = \frac{1}{n_s} \sum_{i=1}^{n_s} v(\boldsymbol{x}_i) h_\eta(\boldsymbol{x}_j - \boldsymbol{x}_i, \boldsymbol{x}_i, a(\boldsymbol{x}_i)), \tag{6}$$

where $\boldsymbol{x}_j$ lies on resampled equispaced grids. Another $\mathcal{H}'_\zeta$ interpolates back on the $n_s$ non-equispaced ones in the same way via the convolution with kernel $h_\zeta$. To reduce the operations to no more than $O(n_s \log n_s)$, the summation is restricted in the neighborhood of $\boldsymbol{x}_i$ and $\boldsymbol{x}_j$, such that $|\mathcal{N}(\boldsymbol{x}_i)| \approx |\mathcal{N}(\boldsymbol{x}_j)| \leq c \log n_s$ with $c$ as a predefined constant determining the neighborhood size of spatial points. We formulate the kernel with a shallow feed-forward neural network. Thanks to the universal approximation of neural networks, the following theorem assures that the interpolation operator can approximate the representation function $v$ arbitrarily well. (For detailed proof, see Appendix. B.) Empirical observations on the convergence of interpolation operators are given in Appendix C.

**Theorem 3.1** (Approximation Theorem of the Adaptive Interpolation)**.** *Assume the setting of* ***Theorem B.2*** *in Appendix. B is satisfied.* $\mu$ *is the probability measure supported on* $D$*. For* $v \in \mathcal{U}$*, suppose* $\mathcal{U} = L^p(D; \mathbb{R}^{d_v})$*, for any* $1 < p < \infty$*. Then, given* $\epsilon > 0$*, there exist a neural network* $h_\eta : \mathbb{R}^d \times \mathbb{R}^d \times \mathbb{R}^{d_a} \to \mathbb{R}^{d_v}$*, such that* $||\hat{v} - v||_{\mathcal{U}} \leq \epsilon$*, where* $\hat{v}(\boldsymbol{x}) = \int_D h_\eta(\boldsymbol{x} - \boldsymbol{y}, \boldsymbol{x}, a(\boldsymbol{y}))v(\boldsymbol{y})d\mu(\boldsymbol{y})$*.*

### 3.3 EXPERIMENTS

**Benchmarks and protocols.** For finite-dimensional operators, we choose Vision Mixers including VIT (Dosovitskiy et al., 2020), GFN (Rao et al., 2021) and MLPMIXER (Tolstikhin et al., 2021) as equispaced problem solvers, with DEEPONET-V and DEEPONET-U as two variants for DeepONet(Lu et al., 2021) and graph spatio-temporal models including DCRNN (Li et al., 2018), AGCRN (Bai et al., 2020) and GCGRU (Seo et al., 2016) as non-equispaced problem solvers. For infinite-dimensional operators, the state-of-the-art FNO (Li et al., 2020d) for equispaced problems and MPPDE (Brandstetter et al., 2022) for non-equispaced problems are chosen. A brief introduction to these models is shown in Appendix. B.1. The widely-used metrics - Mean Absolute Error (MAE) is deployed to measure the performance. The reported mean and standard deviation of metrics are obtained through 5 independent trials.

**Data.** We choose 4 equations in experiments: Korteweg de Vries (KdV) and Burgers' equation for 1-d problem and Darcy Flow and Navier-Stokes (NS) equation for a viscous, incompressible fluid in vorticity form on the unit torus for 2-d PDEs. The total number of instances is 1200, with percentages of 0.7, 0.1 and 0.2 for training, validating and testing, respectively. When evaluating their performance in equispaced scenarios of different resolutions, we can downsample the resolution for training to low-resolution data, e.g. $64 \times 64$ in NS equation. To evaluate their performance in non-equispaced scenarios of different meshes, we randomly choose $n_s$ spatial points for training. Details are given in Appendix. B.2.

Table 1: MAE($\times 10^{-3}$) comparison with vision mixer benchmarks.

| | Burgers' ($n_t = 10$) | | | Darcy Flow | | | NS ($n_t = 1$) | | | NS ($n_t = 10$) | | |
|---|---|---|---|---|---|---|---|---|---|---|---|---|
| $r$ | 512 | 512 | 1024 | 64 | 128 | 256 | 64 | 64 | 128 | 64 | 64 | 128 |
| $n_t'$ | 10 | 40 | 20 | 1 | 1 | 1 | 10 | 40 | 20 | 10 | 40 | 20 |
| VIT | 0.5042 | 2.4269 | 1.5327 | 0.5073 | 0.9865 | 1.1078 | 9.3797 | 22.8565 | 15.7398 | 3.9609 | 12.3433 | 9.3010 |
| MLPMIXER | 0.1973 | 0.4210 | 0.3303 | 0.4970 | 0.8909 | 0.9125 | 7.5246 | 15.8632 | 14.9360 | 3.1530 | 7.9291 | 7.7410 |
| GFN | 0.2383 | 0.4187 | 0.3500 | 0.4739 | 0.8659 | 0.9618 | 3.5524 | 10.2250 | 6.3976 | 1.7396 | 5.4464 | 3.1261 |
| FNO | 0.0978 | 0.1815 | **0.1430** | 0.4289 | 0.7086 | 0.9075 | 3.3425 | 8.9857 | 4.4627 | 2.4076 | 7.6979 | 3.7001 |
| DEEPONET-U | 0.4471 | 1.9624 | 0.6541 | 0.3753 | 0.9488 | 0.9692 | 7.4912 | 16.0440 | 14.3476 | 3.4436 | 10.2950 | 7.1394 |
| DEEPONET-V | 0.4782 | 2.1707 | 1.6131 | 0.5119 | 0.9614 | 1.3216 | 8.6986 | 18.5561 | 16.0587 | 3.9745 | 12.3314 | 9.3471 |
| NFS | **0.0958** | **0.1708** | 0.1474 | **0.1497** | **0.2254** | **0.4216** | **1.7425** | **4.7882** | **2.6988** | **0.8636** | **3.1122** | **1.8406** |

**Performance comparison.** In this part, for time-dependent PDEs, our target is to map the observed physical quantities from initial condition $u(\boldsymbol{X}, \boldsymbol{T}) \in \mathbb{R}^{n_s \times n_t}$, where $\boldsymbol{T} = \{t_i : t_i < T\}_{1 \leq i \leq n_t}$, to quantities at some later time $u(\boldsymbol{X}, \boldsymbol{T'}) \in \mathbb{R}^{n_s \times n_t'}$, where $\boldsymbol{T'} = \{t_i : T < t_i < T'\}_{1 \leq i \leq n_t'}$. We set the input timestamp number $n_t$ as 1 (initial state to future dynamics) and 10 (sequence to sequence), and prediction horizon $n_t'$ as 10, 20 and 40 as short-, mid- and long-term settings. For Darcy Flows, which are independent of time, we directly build an operator to map $a$ to $u$. In equispaced scenarios, the resolution is denoted by $r^d = n_s$, where $d$ is the spatial dimension. In non-equispaced scenarios, the spatial points number is denoted by $n_s$. The comparison of methods are shown in Table. 1, Table. B3 and Fig. B2, and detailed results are given in Appendix. B.3. It can be concluded that *(1)* All of the evaluated Vision Mixers are able to model the dynamical systems effectively, in spite of FNO as the only discretization-invariant model; *(2)* In equispaced scenarios, the proposed NFS obtains the lowest error in most 1-d PDE settings, and in solving 2-d PDEs, its superiority over other Vision Mixers are significant, with $42.85\%$ improvements on MAE according to the trials of NS ($r = 64, n_t = 10, n_t' = 40$). *(3)* In non-equispaced scenarios, the evaluated graph spatio-temporal models' performance is unsatisfactory, especially in NS equations. In comparison, NFS achieves comparable high accuracy to the equispaced scenarios, for instance, according to columns of NS ($r = 64, n_t = 10, n_t' = 40$) with ($n_s = 4096, n_t = 10, n_t' = 40$).

**Mesh-invariance evaluation and Architecture Analysis.** For the evaluation of mesh-invariance and further analysis on model architecture with more visualization of results, see Appendix. B in detail. We can conclude that *(1)* The errors on unseen meshes are larger than the errors on seen meshes, but acceptable, since they are even lower than other models' prediction error on seen meshes. *(2)* Larger $n_s'$ leads to higher prediction error because a large number of unseen points are likely to disturb the learned token mixing patterns.

## ACKNOWLEDEGEMENT

This work was supported by National Key R&D Program of China (No. 2022ZD0115100), National Natural Science Foundation of China Project (No. U21A20427), and Project (No. WU2022A009) from the Center of Synthetic Biology and Integrated Bioengineering of Westlake University.

## REFERENCES

James Atwood and Don Towsley. Diffusion-convolutional neural networks, 2016.

Jimmy Lei Ba, Jamie Ryan Kiros, and Geoffrey E. Hinton. Layer normalization, 2016. URL https://arxiv.org/abs/1607.06450.

Lei Bai, Lina Yao, Can Li, Xianzhi Wang, and Can Wang. Adaptive graph convolutional recurrent network for traffic forecasting, 2020.

Leah Bar and Nir Sochen. Unsupervised deep learning algorithm for pde-based forward and inverse problems, 2019.

Saakaar Bhatnagar, Yaser Afshar, Shaowu Pan, Karthik Duraisamy, and Shailendra Kaushik. Prediction of aerodynamic flow fields using convolutional neural networks. *Computational Mechanics*, 64(2):525–545, jun 2019. doi: 10.1007/s00466-019-01740-0. URL https://doi.org/10.1007%2Fs00466-019-01740-0.

Kaushik Bhattacharya, Bamdad Hosseini, Nikola B. Kovachki, and Andrew M. Stuart. Model reduction and neural networks for parametric pdes, 2021.

Johannes Brandstetter, Daniel Worrall, and Max Welling. Message passing neural pde solvers, 2022. URL https://arxiv.org/abs/2202.03376.

Umer I. Cheema, Gregory Nash, Rashid Ansari, and Ashfaq Khokhar. Memory-optimized re-gridding architecture for non-uniform fast fourier transform. *IEEE Transactions on Circuits and Systems I: Regular Papers*, 64(7):1853–1864, 2017. doi: 10.1109/TCSI.2017.2681723.

Tianping Chen and Hong Chen. Universal approximation to nonlinear operators by neural networks with arbitrary activation functions and its application to dynamical systems. *IEEE Transactions on Neural Networks*, 6(4):911–917, 1995. doi: 10.1109/72.392253.

Xiangxiang Chu, Zhi Tian, Yuqing Wang, Bo Zhang, Haibing Ren, Xiaolin Wei, Huaxia Xia, and Chunhua Shen. Twins: Revisiting the design of spatial attention in vision transformers, 2021. URL https://arxiv.org/abs/2104.13840.

Michaël Defferrard, Xavier Bresson, and Pierre Vandergheynst. Convolutional neural networks on graphs with fast localized spectral filtering, 2017.

Yihe Dong, Jean-Baptiste Cordonnier, and Andreas Loukas. Attention is not all you need: Pure attention loses rank doubly exponentially with depth, 2021. URL https://arxiv.org/abs/2103.03404.

Alexey Dosovitskiy, Lucas Beyer, Alexander Kolesnikov, Dirk Weissenborn, Xiaohua Zhai, Thomas Unterthiner, Mostafa Dehghani, Matthias Minderer, Georg Heigold, Sylvain Gelly, Jakob Uszkoreit, and Neil Houlsby. An image is worth 16x16 words: Transformers for image recognition at scale, 2020. URL https://arxiv.org/abs/2010.11929.

Weinan E and Bing Yu. The deep ritz method: A deep learning-based numerical algorithm for solving variational problems, 2017.

John Guibas, Morteza Mardani, Zongyi Li, Andrew Tao, Anima Anandkumar, and Bryan Catanzaro. Adaptive fourier neural operators: Efficient token mixers for transformers, 2021. URL https://arxiv.org/abs/2111.13587.

Xiaoxiao Guo, Wei Li, and Francesco Iorio. Convolutional neural networks for steady flow approximation. In *Proceedings of the 22nd ACM SIGKDD International Conference on Knowledge Discovery and Data Mining*, KDD '16, pp. 481–490, New York, NY, USA, 2016. Association for Computing Machinery. ISBN 9781450342322. doi: 10.1145/2939672.2939738. URL https://doi.org/10.1145/2939672.2939738.

Kurt Hornik, Maxwell Stinchcombe, and Halbert White. Multilayer feedforward networks are universal approximators. *Neural Networks*, 2(5):359–366, 1989. ISSN 0893-6080. doi: https://doi.org/10.1016/0893-6080(89)90020-8. URL https://www.sciencedirect.com/science/article/pii/0893608089900208.

Dhiraj D. Kalamkar, Joshua D. Trzaskoz, Srinivas Sridharan, Mikhail Smelyanskiy, Daehyun Kim, Armando Manduca, Yunhong Shu, Matt A. Bernstein, Bharat Kaul, and Pradeep Dubey. High performance non-uniform fft on modern x86-based multi-core systems. In *2012 IEEE 26th International Parallel and Distributed Processing Symposium*, pp. 449–460, 2012. doi: 10.1109/IPDPS.2012.49.

Srinidhi Kestur, Sungho Park, Kevin M. Irick, and Vijaykrishnan Narayanan. Accelerating the nonuniform fast fourier transform using fpgas. In *2010 18th IEEE Annual International Symposium on Field-Programmable Custom Computing Machines*, pp. 19–26, 2010. doi: 10.1109/FCCM.2010.13.

YUEHAW KHOO, JIANFENG LU, and LEXING YING. Solving parametric PDE problems with artificial neural networks. *European Journal of Applied Mathematics*, 32(3):421–435, jul 2020. doi: 10.1017/s0956792520000182. URL https://doi.org/10.1017%2Fs0956792520000182.

Nikola Kovachki, Zongyi Li, Burigede Liu, Kamyar Azizzadenesheli, Kaushik Bhattacharya, Andrew Stuart, and Anima Anandkumar. Neural operator: Learning maps between function spaces, 2021. URL http://tensorlab.cms.caltech.edu/users/anima/pubs/GraphPDE_Journal.pdf.

Yaguang Li, Rose Yu, Cyrus Shahabi, and Yan Liu. Diffusion convolutional recurrent neural network: Data-driven traffic forecasting, 2018.

Zongyi Li, Nikola Kovachki, Kamyar Azizzadenesheli, Burigede Liu, Kaushik Bhattacharya, Andrew Stuart, and Anima Anandkumar. Neural operator: Graph kernel network for partial differential equations, 2020a. URL https://arxiv.org/abs/2003.03485.

Zongyi Li, Nikola Kovachki, Kamyar Azizzadenesheli, Burigede Liu, Kaushik Bhattacharya, Andrew Stuart, and Anima Anandkumar. Multipole graph neural operator for parametric partial differential equations, 2020b.

Zongyi Li, Nikola Kovachki, Kamyar Azizzadenesheli, Burigede Liu, Kaushik Bhattacharya, Andrew Stuart, and Anima Anandkumar. Neural operator: Graph kernel network for partial differential equations, 2020c.

Zongyi Li, Nikola Kovachki, Kamyar Azizzadenesheli, Burigede Liu, Kaushik Bhattacharya, Andrew Stuart, and Anima Anandkumar. Fourier neural operator for parametric partial differential equations, 2020d. URL https://arxiv.org/abs/2010.08895.

Haitao Lin, Zhangyang Gao, Yongjie Xu, Lirong Wu, Ling Li, and Stan. Z. Li. Conditional local convolution for spatio-temporal meteorological forecasting, 2021.

Haitao Lin, Guojiang Zhao, Lirong Wu, and Stan Z. Li. Stonet: A neural-operator-driven spatio-temporal network, 2022. URL https://arxiv.org/abs/2204.08414.

Ze Liu, Yutong Lin, Yue Cao, Han Hu, Yixuan Wei, Zheng Zhang, Stephen Lin, and Baining Guo. Swin transformer: Hierarchical vision transformer using shifted windows, 2021. URL https://arxiv.org/abs/2103.14030.

Lu Lu, Pengzhan Jin, Guofei Pang, Zhongqiang Zhang, and George Em Karniadakis. Learning nonlinear operators via deeponet based on the universal approximation theorem of operators. *Nature Machine Intelligence*, 3:218–229, 2021.

Xiaofeng Mao, Gege Qi, Yuefeng Chen, Xiaodan Li, Ranjie Duan, Shaokai Ye, Yuan He, and Hui Xue. Towards robust vision transformer, 2021. URL https://arxiv.org/abs/2105.07926.

Muzammal Naseer, Kanchana Ranasinghe, Salman Khan, Munawar Hayat, Fahad Shahbaz Khan, and Ming-Hsuan Yang. Intriguing properties of vision transformers, 2021. URL https://arxiv.org/abs/2105.10497.

Shaowu Pan and Karthik Duraisamy. Physics-informed probabilistic learning of linear embeddings of nonlinear dynamics with guaranteed stability. *SIAM Journal on Applied Dynamical Systems*, 19 (1):480–509, Jan 2020. ISSN 1536-0040. doi: 10.1137/19m1267246. URL http://dx.doi.org/10.1137/19M1267246.

Namuk Park and Songkuk Kim. How do vision transformers work?, 2022. URL https://arxiv.org/abs/2202.06709.

Maziar Raissi, Alireza Yazdani, and George Em Karniadakis. Hidden fluid mechanics: Learning velocity and pressure fields from flow visualizations. *Science*, 367(6481):1026–1030, 2020.

Yongming Rao, Wenliang Zhao, Zheng Zhu, Jiwen Lu, and Jie Zhou. Global filter networks for image classification, 2021. URL https://arxiv.org/abs/2107.00645.

Youngjoo Seo, Michaël Defferrard, Pierre Vandergheynst, and Xavier Bresson. Structured sequence modeling with graph convolutional recurrent networks, 2016.

Justin Sirignano and Konstantinos Spiliopoulos. DGM: A deep learning algorithm for solving partial differential equations. *Journal of Computational Physics*, 375:1339–1364, dec 2018. doi: 10.1016/j.jcp.2018.08.029. URL https://doi.org/10.1016%2Fj.jcp.2018.08.029.

Jonathan D. Smith, Kamyar Azizzadenesheli, and Zachary E. Ross. Eikonet: Solving the eikonal equation with deep neural networks, 2020.

Ilya Tolstikhin, Neil Houlsby, Alexander Kolesnikov, Lucas Beyer, Xiaohua Zhai, Thomas Unterthiner, Jessica Yung, Andreas Steiner, Daniel Keysers, Jakob Uszkoreit, Mario Lucic, and Alexey Dosovitskiy. Mlp-mixer: An all-mlp architecture for vision, 2021. URL https://arxiv.org/abs/2105.01601.

Shikhar Tuli, Ishita Dasgupta, Erin Grant, and Thomas L. Griffiths. Are convolutional neural networks or transformers more like human vision?, 2021. URL https://arxiv.org/abs/2105.07197.

Matthew A. Wright and Joseph E. Gonzalez. Transformers are deep infinite-dimensional non-mercer binary kernel machines, 2021. URL https://arxiv.org/abs/2106.01506.

Baosong Yang, Longyue Wang, Derek Wong, Lidia S. Chao, and Zhaopeng Tu. Convolutional self-attention networks, 2019. URL https://arxiv.org/abs/1904.03107.

# A DISCUSSION OF METHODS

**FNO can be regarded as a member of the family of Vision Mixers.** The reason is that a component in an iteration in Eq. (2) can be written as $(R_\phi \cdot \mathcal{F}(v))(\boldsymbol{x}) = R_\phi \cdot \sum_i e^{-2\pi i <\boldsymbol{x}, \boldsymbol{x}_i>} v(\boldsymbol{x}_i)$, because in the equispaced scenarios, $\boldsymbol{x}_i$ can be regarded as lying on the same grids as $\boldsymbol{k}$ after scaling. The kernel $\kappa_\phi$ is parameterized by $\kappa_\phi(\boldsymbol{x}, \boldsymbol{x}_i, v(\boldsymbol{x}), v(\boldsymbol{x}_i)) = e^{-2\pi i <\boldsymbol{x}, \boldsymbol{x}_i>}$ , and the matrix multiplication of $R_\phi$ also performs mixing on channels. Besides, the inverse Fourier transform can also be regarded as token mixing layers, or so-called token demixing layers (Guibas et al., 2021).

**Applicability of Layer-Norm.** As shown in Fig. 2, besides the comparison of the proposed interpolation operator with the traditional ones, a notable difference between the original FNO and FNO layers in our Vision Mixer architecture is the applicability of normalization layers (Layer-Norm) which is usually used in Vision Mixers' architecture. FNO cannot adapt Layer-Norm layers, because the change of resolution will make the trained normalization parameters and spatial points disagree with each other. In comparison, the resampled equispaced points are fixed in our architecture, no matter how the discretization of the input changes. Therefore, the normalization layers can be added, in a similar way to Vision Mixers, bringing considerable improvements (See Sec. B.5).

**Mesh invariance.** In the intermediate layers, which adopt equispaced FNO, the resampled points are fixed in both training and inference process, invariant to the input meshes. In the interpolation layers, the operator $\mathcal{H}_\eta(a)$ is discretization-invariant because the kernel can be inductively obtained by the newly observed signals $a(\boldsymbol{x})$, its coordinate $\boldsymbol{x}$ and resampled spatial points' relative coordinates $\boldsymbol{x}_j - \boldsymbol{x}$. In the same way, $\mathcal{H}'_\zeta(a)$ is also mesh-invariant. This allows the NFS to achieve zero-shot mesh-invariant inference ability, which is demonstrated in Sec. **??**.

**Complexity analysis.** The complexity of FNO is $O(n_s \log n_s + n_s k_{\max})$. In the interpolation layers, because the interpolated values of resampled points are determined by their neighbors, we set the size of each resampled point's neighborhood in $\mathcal{G}$ and observed non-equispaced points's neighborhood in $\mathcal{G}'$ as $|\mathcal{N}(\boldsymbol{x}_i)| \approx |\mathcal{N}(\boldsymbol{x}_j)| \leq c \log(n_s)$, for $1 \leq i \leq n_s, 1 \leq j \leq m_s$. And in this way, the sparsity of the interpolation matrix reduces the complexity of the two interpolation layers to $O(c \cdot n_s \log n_s + c \cdot m_s \log n_s)$. If we set the resampled points number as $n_s$, the overall complexity is $O(2c \cdot n_s \log n_s + n_s \log n_s + n_s k_{\max}) \sim O(n_s \log n_s + n_s k_{\max})$.

**Relation to Vision Mixer.** The interpolation can be compared to patchwise embedding in Vision Mixers. For example, MLPMIXER learns the token mixing patterns adaptively with a feed-forward network, but the high resolution of input images does not permit the global mixing of tokens due to the complexity of $O(n_s^2)$. Therefore, the input images are firstly rearranged into patches, with each patch containing $n_p$ pixels. In this way, the complexity is reduced to $O(n_s^2/n_p^2)$, enabling feasible token mixing. The patchwise embedding is very similar to interpolating the values on resampled points, as the former one first chooses patches' centers as $n_s^2/n_p^2$ resampled points, and 'interpolates' the resampled points by lifting the embedding dimension and the rearranging of their neighbors' values as the interpolated values, rather than using a kernel.

**Relation to multipole graph model.** The adaptively learned interpolation layer in NFS has a similar formulation of multipole graph models (Li et al., 2020b). In multipole graph models, the high-level nodes aggregate messages from their low-level neighbors as $v^{\text{High}}(\boldsymbol{x}_j) = \frac{1}{|\mathcal{N}(\boldsymbol{x}_j)|} \sum_{\boldsymbol{x}_i \in \mathcal{N}(\boldsymbol{x}_j)} v^{\text{Low}}(\boldsymbol{x}_i) h_\eta(\boldsymbol{x}_j, \boldsymbol{x}_i, a(\boldsymbol{x}_j), a(\boldsymbol{x}_i))$. Compared to multipole graph models, the values of high-level resampled equispaced nodes are approximated with low-level non-equispaced nodes' values in NFS, but nodes' values of low levels are given in multipole graphs. This causes differences in multipole graph models' message-passing and NFS's interpolation: In the former one, messages flow circularly among different levels of nodes, while in NFS, messages only exchange twice between the nodes of two levels – one is from low-level non-equispaced nodes to high-level resampled equispaced nodes, and the other is the opposite.

## B APPROXIMATION THEOREM

**Proof of Theorem 3.1.** Our proof is mostly based on Chen & Chen (1995) and Kovachki et al. (2021). For notation simplicity, in the proof, we directly write $\mathcal{H}_\eta(a)$ as $\mathcal{H}_\eta$ as the linear operator.

**Lemma B.1.** *Let $\mathcal{X}$ be a Banach space, and $\mathcal{U} \subseteq \mathcal{X}$ a compact set, and $\mathcal{K} \subset \mathcal{X}$ a dense set. Then, for any $\epsilon > 0$, there exists a number $n \in \mathbb{N}$, and a series of continuous, linear functionals $G_1, G_2, \ldots, G_n \in C(\mathcal{U}; \mathbb{R})$, and elements $\varphi_1, \ldots, \varphi_n \in \mathcal{K}$, such that*

$$\sup_{u \in \mathcal{U}} ||v - \sum_{j=1}^{n} G_j(v)\varphi_j||_{\mathcal{X}} \leq \epsilon \tag{7}$$

The proof is given in **Lemma 7.** in Kovachki et al. (2021), and **Theorem 3.** and **4.** for reference .

**Theorem B.2.** *Let $D \subseteq \mathbb{R}^d$ be compact domain. Let $\mathcal{U}$ be a separable Banach space of real-valued functions on $D$, such that $C(D, \mathbb{R}) \subseteq \mathcal{U}$ is dense. Suppose $\mathcal{U} = L^p(D; \mathbb{R})$ for any $1 < p < \infty$. $\nu$ is a probability measure supported on $\mathcal{U}$ and assume that, $\mathbb{E}_{v \sim \nu}||v||_{\mathcal{U}} < \infty$ for any $v \in \mathcal{U}$. $\mu$ is a probabilistic measure supported on $D$, which defines the inner product of Hilbert space $\mathcal{U}$ as $< f, g >_{\mathcal{U}} = \int_D f(\boldsymbol{x})g(\boldsymbol{x})d\mu(\boldsymbol{x})$. Then, there exists a neural network $h_\eta : \mathbb{R}^d \times \mathbb{R}^d \to \mathbb{R}$ whose activation functions are of the Tauber-Wiener class, such that*

$$||v - \mathcal{H}(v)||_{\mathcal{U}} \leq \epsilon,$$

*where $\mathcal{H}(v)(\boldsymbol{x}) = \int_D h_\eta(\boldsymbol{x}, \boldsymbol{y})v(\boldsymbol{y})d\mu(\boldsymbol{y})$.*

*Proof.* Since $\mathcal{U}$ is a Polish space, we can find a compact set $\mathcal{K}$, such that $\nu(\mathcal{U} \setminus \mathcal{K}) \leq \epsilon$. Therefore, **Lemma B.1** can be applied, to find a number $n \in \mathbb{N}$, a series of continuous linear functionals $G_j \in C(\mathcal{U}; \mathbb{R})$ and functions $\varphi_j \in C(D; \mathbb{R})$ such that

$$\sup_{v \in \mathcal{K}} ||v - \sum_{j=1}^{n} G_j(v)\varphi_j||_{\mathcal{U}} \leq \epsilon.$$

Denote $\hat{\mathcal{H}}_n(v) = \sum_{j=1}^{n} G_j(v)\varphi_j$, and let $1 < q < \infty$ be the Hölder conjugate of $p$. Since $\mathcal{U} = L^p(D; \mathbb{R})$, by Reisz Representation Theorem, there exists functions $g_j \in L^q(D; \mathbb{R})$, such that $G_j(v) = \int_D v(\boldsymbol{x})g_j(\boldsymbol{x})d\mu(\boldsymbol{x})$ for $j = 1, \ldots, n$ and $v \in L^p(D; \mathbb{R})$. By density of $C(D; \mathbb{R})$ in $L^q(D; \mathbb{R})$, we can find functions $\psi_1, \ldots, \psi_n \in C(D; \mathbb{R})$, such that

$$\sup_{j \in \{1, \ldots, n\}} ||\psi_j - g_j||_{L^q(D;\mathbb{R})} \leq \epsilon/n.$$

Then, we define $\tilde{\mathcal{H}}_n : L^p(D; \mathbb{R}) \to C(D; \mathbb{R})$ by

$$\tilde{\mathcal{H}}_n(v) = \sum_{j=1}^{n} \int_D \psi_j(\boldsymbol{y})v(\boldsymbol{y})d\mu(\boldsymbol{y})\varphi_j(\boldsymbol{x}).$$

For the universal approximation (density) (Hornik et al., 1989) of neural networks, we can find a Multi-layer Feedforward network $h_\eta : \mathbb{R}^d \times \mathbb{R}^d \to \mathbb{R}$ whose activation functions are of the Tauber-Wiener class, such that

$$\sup_{\boldsymbol{x}, \boldsymbol{y} \in D} |h_\eta(\boldsymbol{x}, \boldsymbol{y}) - \sum_{j=1}^{n} \psi_j(\boldsymbol{y})\varphi_j(\boldsymbol{x})| \leq \epsilon.$$

Let $\mathcal{H}_\eta(\boldsymbol{x}) = \int_D h_\eta(\boldsymbol{x}, \boldsymbol{y})v(\boldsymbol{y})d\mu(\boldsymbol{y})$. Then, there exists a constant $C_1 > 0$, such that

$$||\hat{\mathcal{H}}_n(v) - \mathcal{H}(v)||_{L^p(D;\mathbb{R})} \leq C_1(||\hat{\mathcal{H}}_n(v) - \tilde{\mathcal{H}}_n(v)||_{L^p(D;\mathbb{R})} + ||\tilde{\mathcal{H}}_n(v) - \mathcal{H}(v)||_{L^p(D;\mathbb{R})}).$$

For the first term, there is a constant $C_2 > 0$, such that

$$\begin{aligned}
||\hat{\mathcal{H}}_n(v) - \tilde{\mathcal{H}}_n(v)||_{L^p(D;\mathbb{R})} &\leq C_2 \sum_{j=1}^{n} || \int_D v(\boldsymbol{y})(g_j(\boldsymbol{y}) - \psi_j(\boldsymbol{y}))d\mu(\boldsymbol{y})\varphi_j||_{L^p(D;\mathbb{R})} \\
&\leq C_2 \sum_{j=1}^{n} ||v(\boldsymbol{y})||_{L^p(D;\mathbb{R})}||g_j(\boldsymbol{y}) - \psi_j(\boldsymbol{y})||_{L^q(D;\mathbb{R})}||\varphi_j||_{L^p(D;\mathbb{R})} \\
&\leq C_3\epsilon||v(\boldsymbol{y})||_{L^p(D;\mathbb{R})},
\end{aligned}$$

for some $C_3 > 0$. And for the second term,

$$||\tilde{\mathcal{H}}_n(v) - \mathcal{H}(v)||_{L^p(D;\mathbb{R})} = || \int_D v(\boldsymbol{y})(\sum_{j=1}^{n} \psi_j(\boldsymbol{y})\varphi_j(\cdot) - h_\eta(\cdot, \boldsymbol{y}))d\mu(\boldsymbol{y})||_{L^p(D;\mathbb{R})}$$
$$\leq |D|\epsilon||v||_{L^p(D;\mathbb{R})},$$

Therefore, there is a constant $C > 0$, such that

$$\int_{\mathcal{U}} ||\hat{\mathcal{H}}_n(v) - \tilde{\mathcal{H}}_n(v)||_{\mathcal{U}} d\nu(v) \leq \epsilon C \mathbb{E}_{v\sim\nu}||v||_{\mathcal{U}}$$

. Because of the assumption that $\mathbb{E}_{v\sim\nu}||v||_{\mathcal{U}} < \infty$, and $\epsilon$ is arbitrary, then

$$||v - \mathcal{H}(v)||_{\mathcal{U}} \leq ||v - \hat{\mathcal{H}}_n(v)||_{\mathcal{U}} + ||\hat{\mathcal{H}}_n(v) - \mathcal{H}(v)||_{\mathcal{U}},$$

the proof is complete. □

**Corollary B.3.** *Define $\mathcal{H}_\eta(v) = \int_D h_\eta(\boldsymbol{x} - \boldsymbol{y}, \boldsymbol{x}, a(\boldsymbol{y}))v(\boldsymbol{y})d\mu(\boldsymbol{y})$, the interpolation operator can also approximate $v$ to any precision $\epsilon$.*

*Proof.* We use a one-layer neural network $h_\eta : D \times D \to \mathbb{R}$ as an example, which is defined as $h_\eta(\boldsymbol{x}, \boldsymbol{y}, a(\boldsymbol{y}) = \sigma(\sum_{i=1}^{d} w_{x,i}x^{(i)} + w_{y,i}y^{(i)} + b)$. We can rewrite it as

$$h_\eta = \sigma(\sum_{i=1}^{d} w_{x,i}(x^{(i)} - y^{(i)}) + (w_{y,i} + w_{x,i})y^{(i)} + \sum_{j=1}^{d_a} w_{a,j}a^{(j)}(\boldsymbol{y}) + b),$$

where $w_{a,j} = 0$. □

**Corollary B.4.** *The **Theorem B.2** and **Corollary B.3** can be extended for $v : D \to \mathbb{R}^{d_v}$, where $d_v > 1$.*

*Proof.* As $v = (v^{(1)}, v^{(2)}, \ldots, v^{(d_v)})$, for each $v^{(j)}$, a single neural network can be used for approximation. Moreover, in implementation, we make $h_\eta$ fully-connected, to improve the expressivity. □

**Remark.** *As $\sum_{\boldsymbol{x}_i \in \boldsymbol{X}} v(\boldsymbol{x}_i)h_\eta(\boldsymbol{x} - \boldsymbol{x}_i, \boldsymbol{x}_i, a(\boldsymbol{x}_i))$ is the unbiased estimation of $\mathbb{E}_{\boldsymbol{y}\sim\mu}(h_\eta(\boldsymbol{x}, \boldsymbol{y})v(\boldsymbol{y}))$, we use the Equation. (6) for the approximation.*

### B.1 Benchmark Method Description

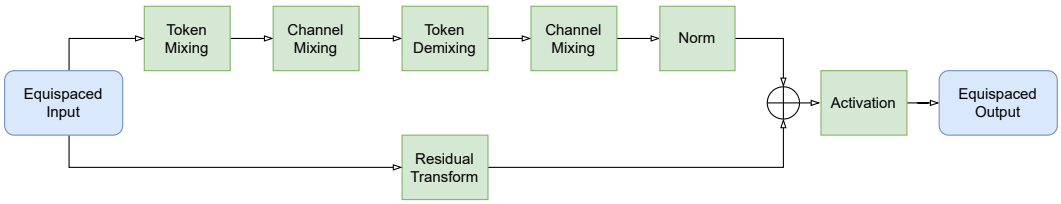


Figure B1: The architecture of Vision Mixers.

**Vision Mixers.** We provide a framework for vision mixers as PDE solvers, including VIT, MLP-Mixer, FNet, GFN, FNO, PFNO and our NFS. The intermediate architecture of mixing layers is shown in Fig. B1. The code of our framework will be released soon. And the resampling and back-sampling methods are stacked before 'Equispaced Input' and 'Equispaced Output'. In this way, the description of the Vision Mixers included in our framework can be described by different modules, as shown in Table. B1. All the trials on Vision Mixers set *embedding size* as 32, *batch size* as 4, *layer number* of the intermediate equispaced mixing layers as 2. In FNO and PFNO, the truncated $K_{\max}$ is set as 16. The *patch size* of Vision Mixers with patchwise embedding are set as $[4, 2]$ in 1-d PDEs and $[4, 4, 2]$ in 2-d PDEs. The interpolation layers in NFS are composed of one layer of feed-forward network whose perceptron unit is equal to $4\times$ *embedding size* of the model.

Table B1: Description of Vison Mixers in the unifying framework module by module.

| Modules | VIT | MLPMIXER | FNET | GFN | FNO | PFNO | NFS |
|---|---|---|---|---|---|---|---|
| Resampling | Patchwise Embedding | Patchwise Embedding | Patchwise Embedding | Patchwise Embedding | Identity | Patchwise Embedding | Interpolation |
| Token Mixing | Attention | MLP | Fourier | Fourier | Fourier | Fourier | Fourier |
| Channel Mixing | Linear | Linear | Linear | Elementwise Product | Low Frequency MatMultiply | Low Frequency MatMultiply | Low Frequency MatMultiply |
| Token Demixing | Identity | Identity | Identity | Inverse Fourier | Inverse Fourier | Inverse Fourier | Inverse Fourier |
| Channel Mixing | Identity | Identity | Identity | Linear | Identity | Identity | Identity |
| Normalization | LayerNorm | LayerNorm | Complex LayerNorm | LayerNorm | Identity | LayerNorm | LayerNorm |
| Residual | Identity | Identity | Identity | Identity | 1x1 Conv | 1x1 Conv | 1x1 Conv |
| Activation | Gelu | Gelu | Complex Gelu | Gelu | Gelu | Gelu | Gelu |
| Back Sampling | Linear+ Rearrange | Linear+ Rearrange | Linear+ Rearrange | Linear+ Rearrange | Identity | Linear+ Rearrange | Interpolation |

**DeepONet Variants.** Since vanilla DeepONet uses MLP as Branch Net, it cannot be implemented in such a high-resolution dataset, because for a resolution like the trial (NS $n_s = 4096, n_t = 10, n'_t = 10$ ), DeepONet assigns each data point a weight parameter in a single MLP, leading the MLP's parameter number reaches $O(n_s^2 n_t^2) \approx 40960^2$ in a single Branch Net, which is infeasible in practice. In the original paper, the spatial point's number in the experiments is set as 40, far less than in the recent Neural Operator's evaluation protocol.

One feasible alternative is to use other architecture to replace the original MLP, thus allowing DeepONet to handle high-resolution data. For example, CNN and Vit. Therefore, we here conduct further experiments on the three equations in the context, to evaluate DeepONet-U (using UNet as the Branch Net) and DeepONet-V (using Vit as the Branch Net) as two variants of vanilla DeepONet for comparison. Note that the architecture of variants of DeepONet are all limited to equispaced data.

**Graph Spatio-Temporal Models.** The evaluated graph spatio-temporal neural networks are based on recurrent neural networks for dynamics modeling, where the spatial dependency is modeled by graph neural networks. The spatial and temporal modules for AGCRN, DCRNN and GCGRU are shown in Table. B2. MPPDE used different architecture, with the pushforward trick used for taining, with *rolling* equaling 1 and *time window* equaling to 10 . All the trials on these graph spatio-tempral models set *embedding size* as 64, except MPPDE as 128. *Batch size* is set as 4. When the graph convolution needs multi-hop message-passing, we set the hop as 2. For MPPDE, the layer number of GNNs is 6. The *embedding dimension* in AGCRN is set as 2.

Table B2: Description of different graph spatio-temporal models

| Methods | Spatial module | Temporal module |
|---|---|---|
| GCGRU Seo et al. (2016) | Cheb Conv Defferrard et al. (2017) | GRU |
| DCRNN Li et al. (2018) | Diff Conv Atwood & Towsley (2016) | GRU |
| AGCRN Bai et al. (2020) | Node Similarity Bai et al. (2020) | GRU |

### B.2 DATA GENERATION

**Burgers' Equation.** The initial condition $u_0(x)$ is generated according to $u_0 \sim N(0.625(-\Delta + 25I)^{-2})$ with periodic boundary conditions. $\nu$ is set as $0.01$. $x \in [0, 1]$ and $t \in [0, 1]$. The spatial resolution is 1024, and time resolution is 200. The dataset generation follows FNO's protocol, which can be downloaded from its source code on official Github.

**KdV Equation.** The equation is written as

$$\partial_t u(x,t) + 3\partial_x u^2(x,t) + \partial_x^3 u(x,t) = 0, \tag{8}$$

where $x \in [0,1]$. The initial condition $u_0(x)$ is calculated as

$$u(x,0) = \sum_{i=1}^{K} 0.5 c_i \cos(0.5\sqrt{c_i + b_i} x - a_i)$$

where $c_i \sim N(0, \sigma_i)$, and $a_i, b_i > 0$. The spatial resolution is 1024. The dataset is generated by `scipy` package, with `fftpack.diff` used as pesudo-differential method and `odeint` used as forward Euler method.

**Darcy Flow.** The equation is written as

$$\begin{aligned} -\nabla(a(\boldsymbol{x})\nabla u(\boldsymbol{x})) &= f(\boldsymbol{x}) & \boldsymbol{x} &\in (0,1)^2 \\ u(\boldsymbol{x}) &= 0 & \boldsymbol{x} &\in \partial[0,1]^2 \end{aligned} \tag{9}$$

The original resolution is $256 \times 256$. $a(\boldsymbol{x})$ is generated by Gaussian random field, and we directly establish the operator to learn the mapping of $a$ to $u$.

**NS Equation.** Our generation of NS Equation is based on FNO's Appendix. A.3.3, which is

$$\begin{aligned} \partial_t w(\boldsymbol{x},t) + u(\boldsymbol{x},t)\cdot\nabla w(\boldsymbol{x},t) &= \nu\Delta w(\boldsymbol{x},t) + f(\boldsymbol{x}), \\ \nabla\cdot u(\boldsymbol{x},t) = 0, \qquad w(\boldsymbol{x},0) &= w_0(\boldsymbol{x}), \end{aligned} \tag{10}$$

where $\boldsymbol{x} \in [0,1]^2, t \in [0,1]$. $u$ is the velocity field, $w = \nabla \times u$ is the vorticity, $w_0$ is the initial vorticity, $\nu \in \mathbb{R}^+$ is the viscosity coefficient, and $f$ is the forcing function which is kept fixed. The original spatial resolution is $128 \times 128$, and time resolution is 200.

### B.3 Complete Results on Model Comparison

Table. B3 and Fig. B2 is a brief demonstration of the model comparison.

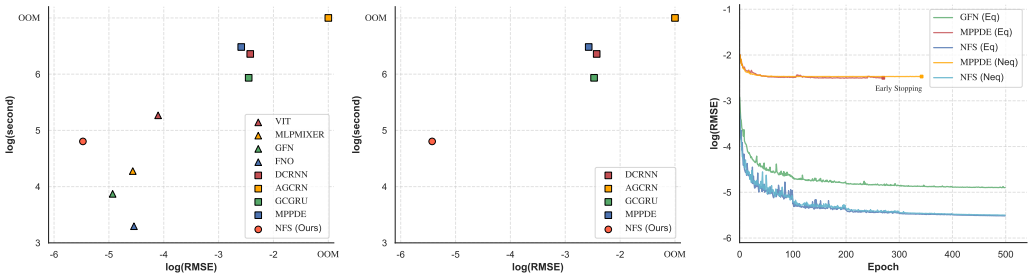


(a) Equispaced comparison (b) Non-equispaced comparison (c) Loss on Validation Set

Figure B2: In (a) and (b), '△' represents Vision Mixers, '□' represents graph spatio-temporal models and '◯' is the proposed NFS. In (c), 'Eq' and 'Neq' mean the methods are trained in equispaced and non-equispaced scenarios respectively.

Table B3: MAE($\times 10^{-3}$) comparison with graph spatio-temporal benchmarks.

| | Burgers' ($n_t = 10$) | | | Darcy Flow | | | NS ($n_t = 1$) | | | NS ($n_t = 10$) | | |
|---|---|---|---|---|---|---|---|---|---|---|---|---|
| $n_s$ | 512 | 512 | 256 | 4096 | 16384 | 1024 | 4096 | 4096 | 1024 | 4096 | 4096 | 1024 |
| $n_t'$ | 10 | 40 | 20 | 1 | 1 | 1 | 10 | 40 | 20 | 10 | 40 | 20 |
| DCRNN | 2.6122 | 8.5880 | 4.6126 | 1.7629 | OOM | 1.8146 | 30.6756 | 88.3382 | 52.1290 | 8.7025 | 59.6602 | 27.1069 |
| AGCRN | 4.6667 | 15.6143 | 10.4900 | 1.7336 | OOM | 1.6938 | OOM | OOM | 59.9393 | OOM | OOM | 42.4197 |
| GCGRU | 1.6643 | 5.7653 | 3.1400 | 1.7403 | OOM | 1.7633 | 28.8537 | 85.9303 | 49.9352 | 6.3570 | 57.2493 | 21.3537 |
| MPPDE | 1.1271 | 4.1213 | 2.4554 | 0.5608 | 0.6384 | 0.6673 | 8.9810 | 54.2387 | 20.7453 | 5.4353 | 42.3057 | 17.5902 |
| NFS | **0.1085** | **0.1983** | **0.1634** | **0.1430** | **0.2379** | **0.1727** | **2.1992** | **4.7865** | **3.9178** | **0.9335** | **3.2768** | **1.8239** |

**Complete results on the four Equations.** Table. B4 give the performance comparison on Darcy flow of both equispaced and non-equispaced scenarios. Table. B5 and B6 gives performance comparison

in equispaced scenarios on the other three time-dependent problems. Table. B7 and B8 gives performance comparison in non-equispaced scenarios on the other three time-dependent problems. In all the tasks except `Darcy Flow`, the depth of layer is set as 2, and $k_{\max} = 16$ in both NFS and FNO. However, we find in `Darcy Flow`, $k_{\max}$ should be set much larger, or the loss will not decrease. In the reported results, $k_{\max} = 32, 64, 128$ in `Darcy Flow`.

Table B4: Performance comparison on Darcy Flow.

| | MAE ($\times 10^{-3}$) | RMSE($\times 10^{-3}$) | MAE($\times 10^{-3}$) | RMSE($\times 10^{-3}$) | MAE($\times 10^{-3}$) | RMSE($\times 10^{-3}$) |
|---|---|---|---|---|---|---|
| | `Darcy Flow` ($r = 64$) | | `Darcy Flow` ($r = 128$) | | `Darcy Flow` ($r = 256$) | |
| VIT | 0.5073±0.0411 | 0.8468±0.0432 | 0.9865±0.0002 | 1.6195±0.0007 | 1.1078±0.0021 | 1.8444±0.0023 |
| MLPMixer | 0.4970±0.0021 | 0.8228±0.0034 | 0.8909±0.0099 | 1.4221±0.0118 | 0.9125±0.0024 | 1.6459±0.0032 |
| GFN | 0.4739±0.0016 | 0.8345±0.0019 | 0.8659±0.0046 | 1.4237±0.0071 | 0.9618±0.0124 | 1.6139±0.0128 |
| FNO | 0.4289±0.0051 | 0.7740±0.0046 | 0.7086±0.0045 | 0.1324±0.0019 | 0.9075±0.0051 | 1.4940±0.0046 |
| NFS | **0.1497**±0.0005 | **0.1962**±0.0007 | **0.2254**±0.0007 | **0.7245**±0.0009 | **0.4216**±0.0033 | **0.8578**±0.0041 |
| | `Darcy Flow` ($n_s = 1024$) | | `Darcy Flow` ($n_s = 4096$) | | `Darcy Flow` ($n_s = 16384$) | |
| DCRNN | 1.8146±0.0060 | 2.6352±0.0029 | 1.7629±0.0003 | 2.5760±0.0001 | OOM | OOM |
| AGCRN | 1.6938±0.0001 | 2.4440±0.0001 | 1.7336±0.0001 | 2.4167±0.0001 | OOM | OOM |
| GCGRU | 1.7633±0.0001 | 2.5696±0.0001 | 1.7403±0.0001 | 2.5363±0.0001 | OOM | OOM |
| MPPDE | 0.6673±0.0009 | 0.9290±0.0012 | 0.5608±0.0053 | 0.8424±0.0051 | 0.6384±0.0005 | 0.8748±0.0005 |
| NFS | **0.1727**±0.0047 | **0.2311**±0.0066 | **0.1430**±0.0007 | **0.1914**±0.0014 | **0.2379**±0.0007 | **0.3489**±0.0009 |

Table B5: Performance comparison with Vision Mixer benchmarks on different equations ($n_t = 1$). Validation loss on `Burgers'` ($n_t = 1$) of VIT, GFN, and FNO does not converge. The results show that the early-stopping occurs in the begining of training.

| Vision Mixers | MAE ($\times 10^{-3}$) | RMSE($\times 10^{-3}$) | MAE($\times 10^{-3}$) | RMSE($\times 10^{-3}$) | MAE($\times 10^{-3}$) | RMSE($\times 10^{-3}$) |
|---|---|---|---|---|---|---|
| | `Burgers'` ($r = 512, n_t' = 10$) | | `Burgers'` ($r = 512, n_t' = 40$) | | `Burgers'` ($r = 1024, n_t' = 20$) | |
| VIT | 201.6539±0.5284 | 231.9138±0.8403 | 183.6696±0.3015 | 210.6237±0.6767 | 195.5858±0.7706 | 224.4712±1.2472 |
| MLPMixer | 201.6547±0.0671 | 231.9163±0.0263 | 183.6535±0.0599 | 210.6160±0.0305 | 195.5960±0.0240 | 224.4791±0.0132 |
| GFN | 201.6557±0.9513 | 231.9122±0.9535 | 183.6674±0.4893 | 210.6165±0.4831 | 195.5918±0.0471 | 224.4736±0.0681 |
| FNO | 201.6527±1.1415 | 231.9119±1.6747 | 183.6696±0.3015 | 210.6299±0.4983 | 195.5902±0.9304 | 224.4723±0.9230 |
| NFS | **0.1806**±0.0005 | **0.2669**±0.0010 | **0.3570**±0.0008 | **0.5340**±0.0009 | **0.4344**±0.0014 | **0.6092**±0.0017 |
| | `KdV` ($r = 512, n_t' = 10$) | | `KdV` ($r = 512, n_t' = 40$) | | `KdV` ($r = 1024, n_t' = 20$) | |
| VIT | 0.2808±0.0006 | 0.3938±0.0009 | 0.3428±0.0012 | 0.6832±0.0016 | 0.3066±0.0003 | 0.5461±0.0003 |
| MLPMixer | 0.2732±0.0054 | 0.4259±0.0088 | **0.3336**±0.0045 | **0.5923**±0.0081 | 0.2872±0.0005 | 0.5235±0.0006 |
| GFN | 0.2587±0.0032 | 0.3490±0.0056 | 0.3086±0.0223 | 0.5952±0.0338 | 0.2011±0.0074 | 0.3464±0.0063 |
| FNO | 0.2619±0.0069 | 0.3849±0.0107 | 0.5608±0.0053 | 0.8424±0.0051 | 0.3925±0.0079 | 0.4623±0.0087 |
| NFS | **0.2514**±0.0008 | **0.3776**±0.00011 | 0.4522±0.0013 | **0.6290**±0.0022 | **0.2254**±0.0007 | **0.0745**±0.0010 |
| | `NS` ($r = 64, n_t' = 10$) | | `NS` ($r = 64, n_t' = 40$) | | `NS` ($r = 128, n_t' = 20$) | |
| VIT | 9.3797±0.0421 | 12.9291±0.0703 | 22.8565±0.0935 | 29.1130±0.1428 | 15.7398±0.0757 | 20.6927±0.0664 |
| MLPMixer | 7.5246±0.0080 | 10.4762±0.0096 | 15.8632±0.0375 | 20.1522±0.0604 | 14.9360±0.0305 | 19.3268±0.0635 |
| GFN | 3.5524±0.0057 | 4.7071±0.0088 | 10.2250±0.0331 | 13.0451±0.0704 | 6.3976±0.00345 | 8.2685±0.297 |
| FNO | 3.3425±0.0007 | 5.2566±0.0008 | 8.9857±0.0010 | 14.0171±0.0023 | 4.4627±0.0004 | 6.3047±0.0004 |
| NFS | **1.7425**±0.0017 | **2.2847**±0.0022 | **4.7882**±0.0066 | **6.1508**±0.0042 | **2.6988**±0.0005 | **3.5121**±0.0006 |

NFS fails to model the non-equispaced Burgers' Equation when $n_t$ is set as 1, in which the performance is far from it can achieve in equispaced scenarios. Such problem will be our future work.

Table B6: Performance comparison with Vision Mixer benchmarks on different equations ($n_t = 10$).

| Vision Mixers | MAE ($\times 10^{-3}$) | RMSE($\times 10^{-3}$) | MAE($\times 10^{-3}$) | RMSE($\times 10^{-3}$) | MAE($\times 10^{-3}$) | RMSE($\times 10^{-3}$) |
|---|---|---|---|---|---|---|
| | Burgers' ($r = 512, n_t' = 10$) | | Burgers' ($r = 512, n_t' = 40$) | | Burgers' ($r = 1024, n_t' = 20$) | |
| VIT | 0.5042±0.0114 | 0.7667±0.0225 | 2.4269±0.0288 | 3.7728±0.0431 | 1.5327±0.0314 | 2.4093±0.0408 |
| MLPMixer | 0.1973±0.0070 | 0.2600±0.0097 | 0.4210±0.0084 | 0.5844±0.0101 | 0.3303±0.0077 | 0.4473±0.0086 |
| GFN | 0.2383±0.0082 | 0.3066±0.0114 | 0.4187±0.0079 | 0.5407±0.0090 | 0.3500±0.0062 | 0.4489±0.0081 |
| FNO | 0.0978±0.0019 | **0.1287**±0.0023 | 0.1815±0.0009 | 0.2410±0.0011 | **0.1430**±0.0009 | **0.1871**±0.0010 |
| NFS | **0.0958**±0.0015 | 0.1347±0.0022 | **0.1708**±0.0006 | **0.2351**±0.0009 | 0.1474±0.0026 | 0.1957±0.0034 |
| | KdV ($r = 512, n_t' = 10$) | | KdV ($r = 512, n_t' = 40$) | | KdV ($r = 1024, n_t' = 20$) | |
| VIT | 0.2066±0.0027 | 0.3525±0.0049 | 0.2376±0.0022 | 0.5521±0.0036 | 0.1897±0.0003 | 0.3725±0.0009 |
| MLPMixer | 0.2152±0.0023 | 0.3686±0.0039 | **0.2497**±0.0017 | 0.5400±0.0029 | 0.2062±0.0007 | 0.4429±0.0012 |
| GFN | 0.1530±0.0004 | 0.2607±0.0006 | 0.2691±0.0007 | 0.5451±0.0014 | 0.1984±0.0002 | 0.3869±0.0003 |
| FNO | 0.3230±0.0035 | 1.1105±0.0061 | 0.9605±0.0024 | 2.7500±0.0055 | 0.5929±0.0020 | 1.6473±0.0033 |
| NFS | **0.0678**±0.0002 | **0.1214**±0.0003 | 0.2709±0.0009 | **0.5122**±0.0013 | **0.1576**±0.0003 | **0.3114**±0.0005 |
| | NS ($r = 64, n_t' = 10$) | | NS ($r = 64, n_t' = 40$) | | NS ($r = 128, n_t' = 20$) | |
| VIT | 3.9609±0.0101 | 6.0575±0.0250 | 12.3433±0.0342 | 16.5238±0.0415 | 9.3010±0.0234 | 14.0027±0.0380 |
| MLPMixer | 3.1530±0.0049 | 4.4339±0.0067 | 7.9291±0.0038 | 10.4149±0.0066 | 7.7410±0.0037 | 10.1934±0.0082 |
| GFN | 1.7396±0.0016 | 2.3551±0.0028 | 5.4464±0.0023 | 7.2130±0.0032 | 3.1261±0.0026 | 4.1691±0.0047 |
| FNO | 2.4076±0.0017 | 3.2861±0.0024 | 7.6979±0.0035 | 10.6401±0.0056 | 3.7001±0.0034 | 5.0047±0.0072 |
| NFS | **0.8636**±0.0008 | **1.2264**±0.0011 | **3.1122**±0.0020 | **4.1950**±0.0037 | **1.8406**±0.0003 | **2.5620**±0.0005 |

Table B7: Performance comparison with graph spatio-temporal benchmarks ($n_t = 1$).

| Graph Spatio-Temporal Models | MAE ($\times 10^{-3}$) | RMSE($\times 10^{-3}$) | MAE($\times 10^{-3}$) | RMSE($\times 10^{-3}$) | MAE($\times 10^{-3}$) | RMSE($\times 10^{-3}$) |
|---|---|---|---|---|---|---|
| | Burgers' ($n_s = 512, n_t' = 10$) | | Burgers' ($n_s = 256, n_t' = 20$) | | Burgers' ($n_s = 512, n_t' = 40$) | |
| DCRNN | 277.8393±0.0082 | 346.1716±0.0088 | 292.1712±0.0280 | 368.1883±0.0204 | 298.4096±0.0137 | 373.0938±0.0186 |
| AGCRN | 289.9780±0.0001 | 360.9834±0.0001 | 272.6697±0.3404 | 340.1351±0.5435 | 305.4976±0.2120 | 376.0804±0.2385 |
| GCGRU | 288.4507±0.0246 | 361.1175±0.0512 | 294.9075±0.0005 | 367.4703±0.0004 | 291.0365±0.0265 | 365.1668±0.0827 |
| MPPDE | 24.4997±0.0014 | 34.5123±0.0017 | 25.4357±0.0002 | 31.7015±0.0002 | 25.3311±0.0004 | 33.7808±0.0005 |
| NFS | **16.1860**±0.0016 | **28.1504**±0.0021 | **21.1634**±0.0018 | **33.8976**±0.0018 | **26.0818**±0.0001 | **44.7962**±0.0003 |
| | KdV ($n_s = 512, n_t' = 10$) | | KdV ($n_s = 256, n_t' = 20$) | | KdV ($r = 512, n_t' = 40$) | |
| DCRNN | 1.6855±0.0001 | 3.0875±0.0001 | 3.1267±0.0001 | 4.8662±0.0001 | 5.7387±0.0001 | 8.3752±0.0001 |
| AGCRN | 4.0753±0.0001 | 6.8943±0.0001 | 5.4107±0.0001 | 9.2333±0.0001 | 8.4438±0.0001 | 13.8677±0.0001 |
| GCGRU | 1.6554±0.0001 | 2.6839±0.0001 | 3.0677±0.0001 | 4.6557±0.0001 | 5.8745±0.0001 | 9.4528±0.0001 |
| MPPDE | 1.5452±0.0001 | 2.6774±0.0001 | 2.9929±0.0007 | 5.4582±0.0010 | 3.0101±0.0001 | 4.9946±0.0001 |
| NFS | **0.0816**±0.0012 | **0.1512**±0.0022 | **0.1576**±0.0007 | **0.3114**±0.0018 | **0.3210**±0.0021 | **0.6873**±0.0049 |
| | NS ($n_s = 4096, n_t' = 10$) | | NS ($n_s = 1024, n_t' = 20$) | | NS ($n_s = 4096, n_t' = 40$) | |
| DCRNN | 30.6756±0.0001 | 41.7815±0.0001 | 52.1290±0.0138 | 69.7019±0.0032 | 88.3382±0.0864 | 119.5021±0.0055 |
| AGCRN | OOM | OOM | 59.9393±0.0001 | 79.0434±0.0001 | OOM | OOM |
| GCGRU | 28.8537±0.0019 | 40.1215±0.0008 | 49.9352±0.0028 | 67.5623±0.0014 | 85.9303±0.0731 | 117.9925±0.0172 |
| MPPDE | 8.9810±0.0014 | 12.1595±0.0022 | 20.7453±0.0008 | 32.1098±0.0018 | 54.2387±0.0006 | 90.0190±0.0007 |
| NFS | **2.1992**±0.0021 | **2.8280**±0.0033 | **3.9178**±0.0054 | **5.0182**±0.0080 | **4.7865**±0.0042 | **6.1384**±0.0069 |

Table B8: Performance comparison with graph spatio-temporal benchmarks ($n_t = 10$).

| Graph Spatio-Temporal Models | MAE ($\times 10^{-3}$) | RMSE($\times 10^{-3}$) | MAE($\times 10^{-3}$) | RMSE($\times 10^{-3}$) | MAE($\times 10^{-3}$) | RMSE($\times 10^{-3}$) |
|---|---|---|---|---|---|---|
| | Burgers′ ($n_s = 512, n_t' = 10$) | | Burgers′ ($n_s = 256, n_t' = 20$) | | Burgers′ ($n_s = 512, n_t' = 40$) | |
| DCRNN | 2.6122±0.0014 | 3.8435±0.0019 | 4.6126±0.0015 | 6.8853±0.0033 | 8.5880±0.0020 | 12.7394±0.0037 |
| AGCRN | 4.6667±0.0001 | 6.2791±0.0001 | 10.4900±0.0009 | 13.9810±0.0022 | 15.6143±0.0002 | 21.0937±0.0001 |
| GCGRU | 1.6643±0.0002 | 2.5074±0.0003 | 3.1400±0.0010 | 4.8008±0.0019 | 5.7653±0.0021 | 8.9335±0.0028 |
| MPPDE | 1.1271±0.0004 | 1.8838±0.0007 | 2.4554±0.0003 | 4.4315±0.0006 | 4.1213±0.0006 | 6.1980±0.0009 |
| NFS | **0.1085**±0.0016 | **0.1504**±0.0021 | **0.1634**±0.0018 | **0.2328**±0.0018 | **0.1983**±0.0001 | **0.2775**±0.0003 |
| | KdV ($n_s = 512, n_t' = 10$) | | KdV ($n_s = 256, n_t' = 20$) | | KdV ($r = 512, n_t' = 40$) | |
| DCRNN | 2.3196±0.0001 | 4.1634±0.0001 | 3.4503±0.0005 | 5.7450±0.0003 | 4.9286±0.0010 | 8.3912±0.0008 |
| AGCRN | 3.9350±0.0001 | 6.1166±0.0001 | 5.6631±0.0001 | 8.1191±0.0001 | 8.2893±0.0002 | 11.5684±0.0003 |
| GCGRU | 1.6643±0.0001 | 2.5074±0.0001 | 3.4205±0.0001 | 5.6873±0.0001 | 2.5032±0.0002 | 5.4515±0.0003 |
| MPPDE | 1.4967±0.0003 | 2.6309±0.0002 | 2.9708±0.0027 | 5.3811±0.0050 | 2.4293±0.0006 | 4.9310±0.0005 |
| NFS | **0.0816**±0.0012 | **0.1512**±0.0022 | **0.1576**±0.0007 | **0.3114**±0.0018 | **0.3210**±0.0021 | **0.6873**±0.0049 |
| | NS ($n_s = 4096, n_t' = 10$) | | NS ($n_s = 1024, n_t' = 20$) | | NS ($n_s = 4096, n_t' = 40$) | |
| DCRNN | 8.7025±0.0003 | 12.5238±0.0002 | 27.1069±0.0024 | 39.1259±0.0031 | 59.6602±0.0177 | 88.2946±0.0146 |
| AGCRN | OOM | OOM | 42.4197±0.0006 | 60.5375±0.0008 | OOM | OOM |
| GCGRU | 6.3570±0.0001 | 9.7306±0.0002 | 21.3537±0.0026 | 32.9674±0.0033 | 57.2493±0.0085 | 84.1847±0.0106 |
| MPPDE | 5.4353±0.0041 | 7.8838±0.0037 | 17.5902±0.0013 | 25.9372±0.0016 | 42.3057±0.0066 | 76.3374±0.0069 |
| NFS | **0.9335**±0.0011 | **1.3254**±0.0012 | **1.8239**±0.0012 | **2.5291**±0.0008 | **3.2768**±0.0026 | **4.3988**±0.0009 |

### B.4 MESH-INVARIANT EVALUATION AND ARCHITECTURE ANALYSIS

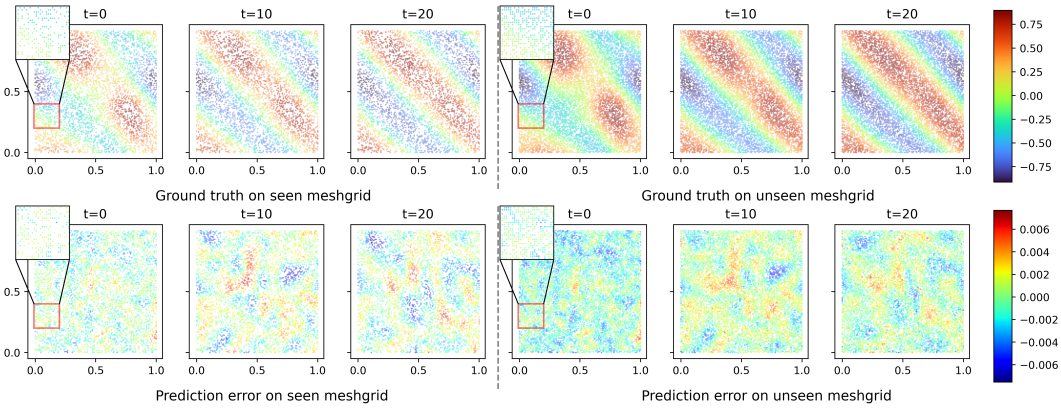


Figure B3: Visualization on non-equispaced NS equation: The training mesh ($n_s = 4096$) differs from the mesh in inference process ($n'_s = 8192$). Appendix. B.9 gives more visualization.

Table B9: Results on NS equation: MAE($\times 10^{-3}$) of NFS and different variants of NFS on seen and unseen meshes. 'Flex + LN' is the proposed NFS. 'Flex' represents the flexible interpolation layer defined in Eq. (6), 'LN' is the Layer-Norm and 'Gaus' is the predefined Gaussian interpolation. Appendix. B.4 gives details and results on other equations.

| | $(n_s = 4096, n_t = 10, n'_t = 10)$ | | | $(n_s = 1024, n_t = 10, n'_t = 20)$ | | | $(n_s = 4096, n_t = 10, n'_t = 40)$ | | |
|---|---|---|---|---|---|---|---|---|---|
| $n'_s$ | Flex + LN | Gaus + LN | Flex + ~~LN~~ | Flex + LN | Gaus + LN | Flex + ~~LN~~ | Flex + LN | Gaus + LN | Flex + ~~LN~~ |
| $n_s$ | 0.9335 | 1.6341 | 1.2138 | 1.8239 | 2.1976 | 2.5119 | 3.2768 | 3.6422 | 5.6761 |
| $2n_s$ | 0.9731 | 2.8589 | 1.4882 | 2.3530 | 3.7465 | 7.0203 | 3.5439 | 3.9092 | 5.8975 |
| $3n_s$ | 1.1071 | 3.4513 | 1.6384 | 2.5179 | 5.7712 | 7.9177 | 3.6584 | 4.2102 | 6.6622 |
| $4n_s$ | 1.1015 | 3.4357 | 1.6975 | 2.5919 | 5.5990 | 7.1962 | 3.6608 | 4.2628 | 6.6951 |

**Mesh-invariance evaluation.** We use $(u(\boldsymbol{X}, \boldsymbol{T}), u(\boldsymbol{X}, \boldsymbol{T'}))$ as the training set, and evaluate the model's performance of mesh-invariant inference ability on $\boldsymbol{X'}$, where $|\boldsymbol{X'}| = n'_s$. $\boldsymbol{X'}$ is a different mesh with $\boldsymbol{X} \subseteq \boldsymbol{X'}$. The visualization results of NS ($n_s = 4096, n'_t = 40$) are shown in Fig. B3. For a fixed $n'_s$, we randomly sampled different $\boldsymbol{X'}$ for 100 times, to get the mean errors and standard deviations (given in Appendix. B.4) of different spatial meshes. We can conclude from Table. B9 that *(1)* The errors on unseen meshes are larger than the errors on seen meshes, showing the overfitting effects. However, the errors on unseen meshes are acceptable, since they are even lower than other models' prediction error on seen meshes. *(2)* Larger $n'_s$ leads to higher prediction error because a large number of unseen points are likely to disturb the learned token mixing patterns. On the other hand, NS ($n_s = 1024, n'_t = 10$) implies that small spatial point numbers of training meshes ($n_s$) hinder model's generalizing ability on unseen meshes, due to excessive loss of spatial information.

### B.5 ARCHITECTURE ANALYSIS

Two modules in NFS differ from FNO. The first is the interpolation layers at the beginning and the end of the architecture. The second is the extra Layer-Norm in the FNO layers, which can be applicable in NFS thanks to its fixed resampled equispaced points, but inapplicable to FNO for preserving its resolution-invariance. We aim to figure out what makes NFS outperform FNO.

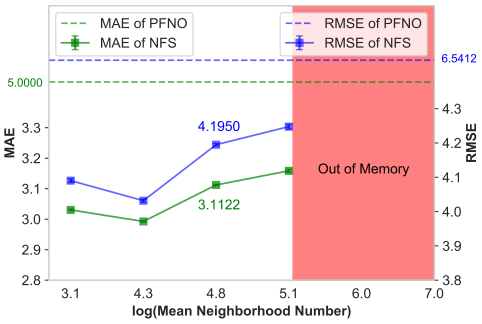


Figure B4: Effects of neighborhood sizes on NS ($r = 64, n'_t = 10, n'_t = 40$).

**Effects of neighborhood sizes.** It is widely believed that modeling the long-range dependency among tokens brings improvements (Naseer et al., 2021; Tuli et al., 2021; Mao et al., 2021). By contrast, some local kernel methods demonstrate their superiority (Yang et al., 2019; Liu et al., 2021; Chu

et al., 2021; Park & Kim, 2022). For this reason, we first conjecture that the large neighborhood sizes in the interpolation layer are conducive to predictive performance. Besides, as demonstrated in Sec. A, the patchwise embedding in Vision Mixers can be an analogy to the resampling and interpolating, so we further establish a patchwise FNO (PFNO), with patch size equaling to $4$ and $[4, 4]$ in 1-d and 2-d PDE problems, equivalent to each resampled points aggregating 4 and 16 points in spatial domains in 1-d and 2-d situations respectively. Layer-Norm is stacked in the FNO layers in PFNO, for a fair comparison. Results of Fig. B4 show that the long-range dependency may even compromise the performance, as larger mean neighborhood sizes often cause higher errors. However, no matter how large is the neighbor size, the NFS outperforms PFNO. Therefore, we rule out the possibility of performance gains brought form large neighborhood sizes and suppose that proposed kernel interpolation layers are the key, and is superior to the simple patchwise embedding methods.

The effects of mean neighborhood size on the predictive performance on `Burgers'` ($n_s = 512, n_t = 10, n_t' = 40$) and `KDV` ($n_s = 512, n_t = 10, n_t' = 40$) are shown in Fig. B5.

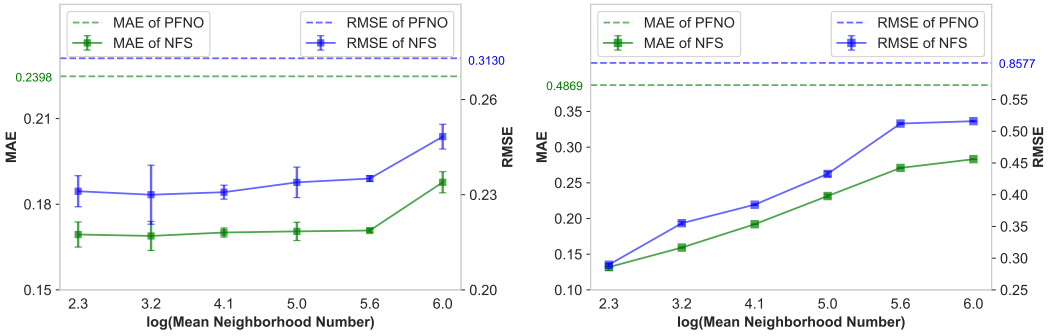


(a) `Burgers'` ($n_s = 512, n_t' = 40$). (b) `KdV` ($n_s = 512, n_t' = 40$).

Figure B5: The change of MAE and RMSE of NFS with the increase of neighborhood size on `Burgers'` ($n_s = 512, n_t = 10, n_t' = 40$) and `KdV` ($n_s = 512, n_t = 10, n_t' = 40$). PFNO is the baseline.

**Benefits from learned interpolation kernel.** Since the kernel interpolation is likely to hold the key to improvements, we investigate the performance gains brought from adaptively learned interpolation kernels over the predefined one (See Fig. 2). We use an inflexible Gaussian kernel $h(\boldsymbol{x}_j - \boldsymbol{x}_i) = \beta \exp(-(\boldsymbol{x}_j - \boldsymbol{x}_i - \boldsymbol{\mu})^T (\Gamma)^{-1} (\boldsymbol{x}_j - \boldsymbol{x}_i - \boldsymbol{\mu}))$ as a predefined one as discussed in Sec. 3.1, where $\Gamma = \mathrm{diag}(\gamma^{(1)}, \dots, \gamma^{(d)})$, and $\boldsymbol{\mu} \in \mathbb{R}^d$, $\gamma^{(1)}, \dots, \gamma^{(d)}, \beta \in \mathbb{R}^+$ are learnable parameters. By setting all the other modules and the interpolation neighborhood sizes as the same, we compare performance on different meshes of the two interpolation kernels in Table. B9 (Gaus + LN), where the adaptively learned kernels achieve better accuracy.

**Benefits from normalization layers.** Previous works demonstrated the normalization is necessary for network architecture, for fast convergence and stable training (Dong et al., 2021; Ba et al., 2016). A notable difference between NFS and FNO is that the Layer-Norm can be implemented in NFS's layers without disabling its discretization-invariance. The improvements brought from the normalization layers are given in Table. B9 (Flex + ~~LN~~), where the performance gap is obvious on unseen meshes.

### B.6 Non-equispaced Vision Mixers

Since NFS can be regarded as a combination of our interpolation layers with the revised FNO, our interpolation layers can also be implemented in the other Vision Mixers, so that these methods are equipped with the ability to handle non-equispaced data. Details are given in Appendix. B.7. We find that *(1)* From Table. B12 and Table. 1, the degeneration of performance is obvious in other Vision Mixers. In comparison, FNO as intermediate equispaced layers, truncates the high frequency in its channel mixing and retains the low frequency shared by both resampled and original signals, so the loss of accuracy in non-equispaced scenarios is tiny in our NFS; *(2)* Although the performance on

unseen meshes is more stable in these non-equispaced Vision Mixers, the performance gap is still large, according to Table. B12 and Table. B9.

Table B10: Mesh-invariant performance of NFS on Burgers' and KdV equations $(n_t = 10)$.

| | MAE ($\times 10^{-3}$) | RMSE($\times 10^{-3}$) | MAE($\times 10^{-3}$) | RMSE($\times 10^{-3}$) |
|---|---|---|---|---|
| | Burgers' ($n_s = 512, n_t = 10, n'_t = 40$) | | KdV ($n_s = 512, n_t = 10, n'_t = 40$) | |
| $\boldsymbol{X}$ | 0.1983±0.0001 | 0.2775±0.0002 | 0.3210±0.0021 | 0.6873±0.0049 |
| $n'_s = 1.3n_s$ | 0.2371±0.0034 | 0.3143±0.0041 | 0.3769±0.0030 | 0.7805±0.0077 |
| $n'_s = 1.7n_s$ | 0.2898±0.0113 | 0.3742±0.0102 | 0.4084±0.0072 | 0.8419±0.0174 |
| $n'_s = 2.0n_s$ | 0.3052±0.0098 | 0.4180±0.0100 | 0.4111±0.0042 | 0.8471±0.0074 |

Table B11: Performance of NFS with its variants of NS equations $(n_t = 10)$ on unseen meshes.

| | MAE ($\times 10^{-3}$) | RMSE($\times 10^{-3}$) | MAE($\times 10^{-3}$) | RMSE($\times 10^{-3}$) | MAE($\times 10^{-3}$) | RMSE($\times 10^{-3}$) |
|---|---|---|---|---|---|---|
| Flex + LN | NS ($n_s = 4096, n'_t = 10$) | | NS ($n_s = 1024, n'_t = 20$) | | NS ($n_s = 4096, n'_t = 40$) | |
| $\boldsymbol{X}$ | 0.9335±0.0011 | 1.3254±0.0012 | 1.8239±0.0012 | 2.5291±0.0008 | 3.2768±0.0026 | 4.3988±0.0009 |
| $n'_s = 2n_s$ | 0.9731±0.0034 | 1.5042±0.0057 | 2.3530±0.0051 | 3.3320±0.0074 | 3.5439±0.0085 | 4.7904±0.0168 |
| $n'_s = 3n_s$ | 1.1071±0.0021 | 1.5716±0.0038 | 2.5179±0.0089 | 3.5477±0.0125 | 3.6584±0.0180 | 4.8858±0.0246 |
| $n'_s = 4n_s$ | 1.1015±0.0000 | 1.5627±0.0000 | 2.5919±0.0064 | 3.6526±0.0071 | 3.6608±0.0000 | 4.9521±0.0000 |
| | MAE ($\times 10^{-3}$) | RMSE($\times 10^{-3}$) | MAE($\times 10^{-3}$) | RMSE($\times 10^{-3}$) | MAE($\times 10^{-3}$) | RMSE($\times 10^{-3}$) |
| Gaus + LN | NS ($n_s = 4096, n'_t = 10$) | | NS ($n_s = 1024, n'_t = 20$) | | NS ($n_s = 4096, n'_t = 40$) | |
| $\boldsymbol{X}$ | 1.6341±0.0034 | 2.1992±0.0042 | 2.1976 ±0.0065 | 3.0219±0.0090 | 3.6422±0.0026 | 5.0097±0.0039 |
| $n'_s = 2n_s$ | 2.8589±0.0062 | 4.0562±0.0126 | 3.7465±0.0041 | 5.1308±0.0097 | 3.9092±0.0041 | 5.2402±0.0075 |
| $n'_s = 3n_s$ | 3.4513±0.0168 | 4.5199±0.0377 | 5.7712±0.0123 | 5.7137±0.0199 | 4.2102±0.0082 | 5.5057±0.0138 |
| $n'_s = 4n_s$ | 3.4357±0.0000 | 4.7382±0.0000 | 5.5990±0.0066 | 5.5958±0.0049 | 4.2628±0.0000 | 5.7679±0.0000 |
| | MAE ($\times 10^{-3}$) | RMSE($\times 10^{-3}$) | MAE($\times 10^{-3}$) | RMSE($\times 10^{-3}$) | MAE($\times 10^{-3}$) | RMSE($\times 10^{-3}$) |
| Flex + ~~LN~~ | NS ($n_s = 4096, n'_t = 10$) | | NS ($n_s = 1024, n'_t = 20$) | | NS ($n_s = 4096, n'_t = 40$) | |
| $\boldsymbol{X}$ | 1.2138±0.0030 | 1.7293±0.0047 | 2.5119±0.0036 | 3.4923±0.0058 | 4.2083±0.0037 | 5.6761±0.0092 |
| $n'_s = 2n_s$ | 1.4882±0.0146 | 2.1681±0.0300 | 7.0203±0.0203 | 10.6096±0.0345 | 5.8975±0.0060 | 8.7704±0.0189 |
| $n'_s = 3n_s$ | 1.6384±0.0088 | 2.4130±0.0169 | 7.9177±0.0059 | 11.9825±0.0118 | 6.6622±0.0063 | 9.5874±0.0131 |
| $n'_s = 4n_s$ | 1.6975±0.0000 | 2.5008±0.0000 | 7.1962±0.0101 | 10.8860±0.0098 | 6.6951±0.0000 | 9.6334±0.0000 |

The mesh-invariant evaluation on Burgers' and KDV Equations of NFS are given in Table. B10. In Table. B10, when the spatial resolution is just 512, inference performance on unseen meshes deteriorates. This result also validates our conclusion *(2)* in the fourth paragraph in Sec. 3.3.

Besides, we give a full evaluation on mesh-invairance of NFS in NS equation, with its variants as a detailed results corresponding to Table. B11.

### B.7 Interpolation with Other Vision Mixers

We conduct experiments on non-equispaced NS equations with the combination of our interpolation layers and other Vision Mixers to figure out if they can achieve camparable performance.

Table B12: Performance of different Vision Mixers combined with the interpolation layers in non-equispaced scenarios on NS equations ($n_t = 10$).

| | MAE ($\times 10^{-3}$) | RMSE($\times 10^{-3}$) | MAE($\times 10^{-3}$) | RMSE($\times 10^{-3}$) | MAE($\times 10^{-3}$) | RMSE($\times 10^{-3}$) |
|---|---|---|---|---|---|---|
| VIT | NS ($n_s = 4096, n'_t = 10$) | | NS ($n_s = 1024, n'_t = 20$) | | NS ($n_s = 4096, n'_t = 40$) | |
| $\boldsymbol{X}$ | OOM | OOM | OOM | OOM | OOM | OOM |
| | MAE ($\times 10^{-3}$) | RMSE($\times 10^{-3}$) | MAE($\times 10^{-3}$) | RMSE($\times 10^{-3}$) | MAE($\times 10^{-3}$) | RMSE($\times 10^{-3}$) |
| MLPMIXER | NS ($n_s = 4096, n'_t = 10$) | | NS ($n_s = 1024, n'_t = 20$) | | NS ($n_s = 4096, n'_t = 40$) | |
| $\boldsymbol{X}$ | 6.1854±0.0012 | 8.1556±0.0018 | 9.4593±0.0028 | 12.1316±0.0022 | 10.1862±0.0045 | 13.1548±0.0051 |
| $n'_s = 2n_s$ | 8.1573±0.0126 | 11.2258±0.0147 | 12.0706±0.0132 | 14.9460±0.0159 | 10.6003±0.0127 | 13.6872±0.0238 |
| $n'_s = 3n_s$ | 8.1952±0.0088 | 11.3840±0.0171 | 14.9910±0.0094 | 17.8415±0.0110 | 10.5633±0.0140 | 13.6394±0.0147 |
| $n'_s = 4n_s$ | 8.7773±0.0000 | 11.3313±0.0000 | 14.9517±0.0125 | 17.7857±0.0199 | 10.5414±0.0000 | 13.6106±0.0000 |
| | MAE ($\times 10^{-3}$) | RMSE($\times 10^{-3}$) | MAE($\times 10^{-3}$) | RMSE($\times 10^{-3}$) | MAE($\times 10^{-3}$) | RMSE($\times 10^{-3}$) |
| GFN | NS ($n_s = 4096, n'_t = 10$) | | NS ($n_s = 1024, n'_t = 20$) | | NS ($n_s = 4096, n'_t = 40$) | |
| $\boldsymbol{X}$ | 12.2373±0.0091 | 16.2902±0.0133 | 10.2768±0.0084 | 13.7852±0.0078 | 14.7765±0.0055 | 19.4872±0.0106 |
| $n'_s = 2n_s$ | 13.7752±0.0164 | 18.3108±0.0181 | 17.7216±0.0225 | 24.1397±0.0371 | 15.9083±0.0235 | 21.0041±0.0256 |
| $n'_s = 3n_s$ | 13.7054±0.0122 | 18.2192±0.0184 | 17.8238±0.0112 | 24.2783±0.0196 | 15.8986±0.0156 | 20.9943±0.0158 |
| $n'_s = 4n_s$ | 13.7140±0.0000 | 18.2271±0.0000 | 17.8207±0.0105 | 24.2833±0.0141 | 15.8736±0.0000 | 20.9772±0.0000 |

### B.8 COMPLEXITY COMPARISON

We here first give Table. B13 to show the complexity of time and memory of all the evaluated methods on NS ($r = 64, n_t = 10, n'_t = 40$).

Table B13: comparison on complexity of the evaluated methods

| Type | Methods | Time/Epoch | Peak Memory | Parameter Number |
|---|---|---|---|---|
| Graph Spatio-Temporal Model | GCGRU | $6'18''$ | 8660MB | 74945 |
| | DCRNN | $9'38''$ | 11120MB | 148673 |
| | AGCRN | OOM | OOM | OOM |
| | MPPDE | $10'54''$ | 23333MB | 622161 |
| Vision Mixer | VIT | $3'14''$ | 32166MB | 773217 |
| | MLPMIXER | $1'12''$ | 4421MB | 79749953 |
| | GFN | $48''$ | 3296MB | 1361729 |
| | FNO | $27''$ | 3748MB | 6299425 |
| | PFNO | $43''$ | 3380MB | 9742145 |
| | NFS | $2'02''$ | 31938MB | 37891937 |

Table B14: Detailed complexity of NFS

| Interpolation on Resampled Points | | |
|---|---|---|
| Neighbor Searching | Kernel Calculation | Weighted Summation |
| 3522MB | 3102MB | 6884MB |
| **Interpolation back on Original Points** | | |
| Neighbor Searching | Kernel Calculation | Weighted Summation |
| 2506MB | 2754MB | 6884MB |

It demonstrates that our method has comparable efficiency to Vision Mixers. For the graph spatial-temporal models, they suffer from the recurrent network structures and thus are extremely time-consuming while the parameter number is small, limiting their flexibility.

**Time.** However, once we compare the used time in PFNO and NFS, we will find that the interpolation layers are considerably time-consuming. Another module that cost time complexity is the normalization layer, as the original FNO does not include Layer-Norm in its architecture, but it is

stacked in PFNO. Theoretically, PFNO handles down-sampled grids in a low resolution, because of the patchwise embedding. However, it takes more time than FNO. Therefore, we conclude that the time complexity brought from Layer-Norm is very significant, but it is affordable because of the performance improvements.

**Memory.** Besides, the operation of searching for each spatial point's neighborhood and calculating weighted summation in Eq. (9) and Eq. (10) are very memory-consuming. We test it on the same experiment, and give the memory usage of different models in forward process, as shown in Table. B14. The memory cost in backward process is 6902MB.

### B.9 More Visualization

Here we provide more visualization results on the three equations. See Fig. B6, Fig. B7 and Fig. B8.

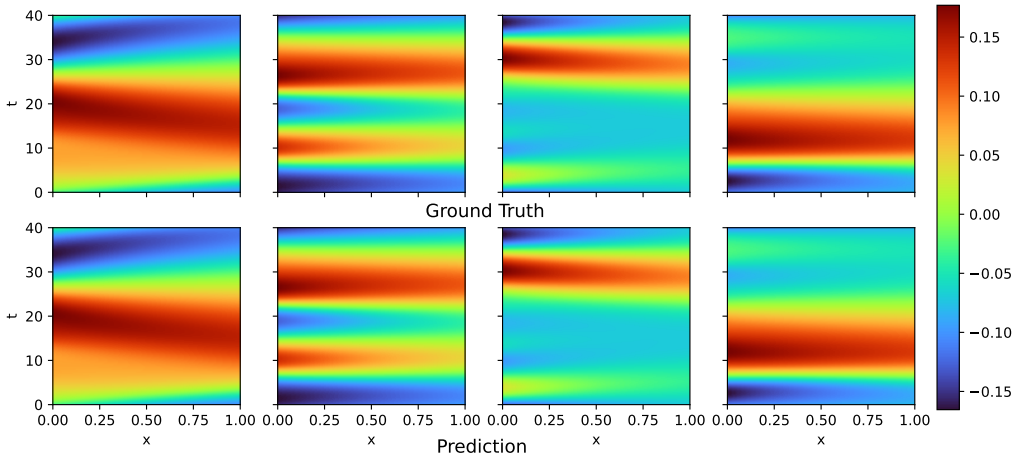


Figure B6: Visualization on equispaced Burgers' equation.

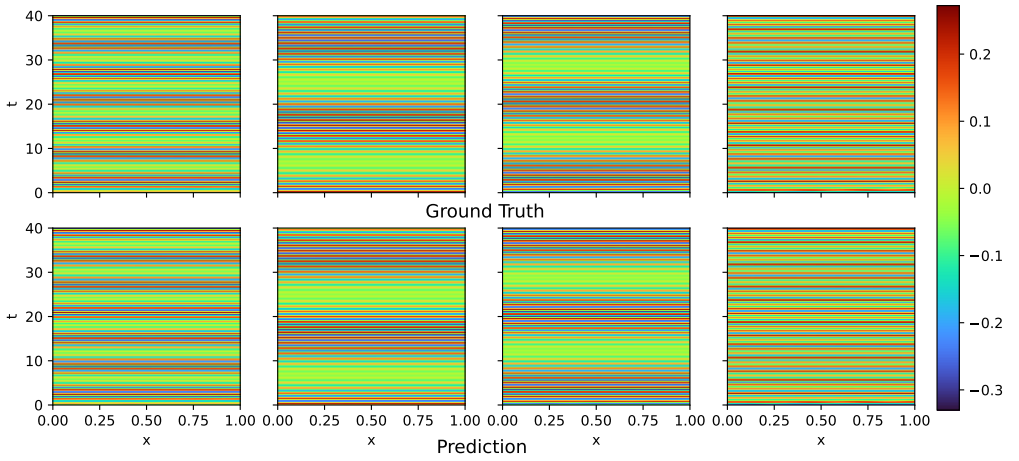


Figure B7: Visualization on equispaced KdV equation.

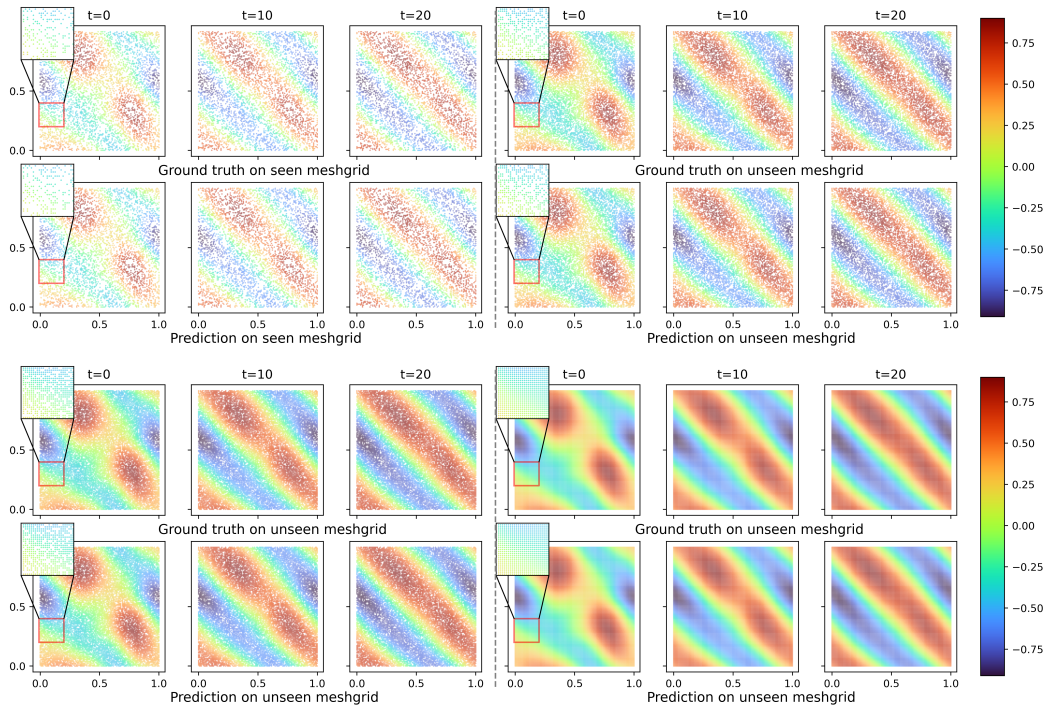


Figure B8: Visualization on non-equispaced NS equation: The training mesh ($n_s = 4096$ in upper-left) is different from the meshes in inference process ($n'_s = 8192$ in upper-right, $n'_s = 12288$ in lower-left and $n's = 16384$ in lower-right).

## C Empirical observation for Theorem 3.1

In Sec. 3.2, Theorem 3.1 is proved to assure the expressivity of NFS. However, no further evidence gives the assurance of the convergence of the kernel interpolation. Here we conduct empirical study to give some clues.

We conduct experiments on NS equation with $n_s = 4096, n_t = 10, n'_t = 40$. In a single trial, NFS is trained with fixed meshes. We repeated the trials 10 times with different meshes, and then give the one-v.s.-all deviations of the representation states calculated by

$$\text{Diff} = \frac{1}{90} \sum_{i \neq j, i,j=1}^{10} \frac{1}{m_s, n'_t} || \frac{|H_i - H_j|}{|H_i| + |H_j|} ||_1,$$

where $H_i$ is the representation states of the shape $[\sqrt{m_s}, \sqrt{m_s}, n'_t]$, and $|\cdot|$ is the element-wise absolute value, and $||\cdot||_1$ is the 1-norm of the matrix. If the Diff is small in the beginning and end, it can be inferred that the interpolation kernel function converges to a similar mapping since the final predictions are close to ground truth in these experiments, and the inputs are sampled from the same instance of PDEs. We give the Diff before the first FNO and after the final of FNO layers in Table. C1. The small values indicate that the trained model usually has similar representation states. Figure. C1 and C2 give visualizations of representation states obtained by one instance of NS equation in two different trials. It indicates that the differences are getting smaller during the training.

Table C1: The defined Diff calculated by different epochs.

| Epoch | $\text{Diff}_{\text{begin}}$ | $\text{Diff}_{\text{end}}$ |
|---|---|---|
| 0 | 0.0676 | 0.0978 |
| 500 | 0.0102 | 0.0353 |

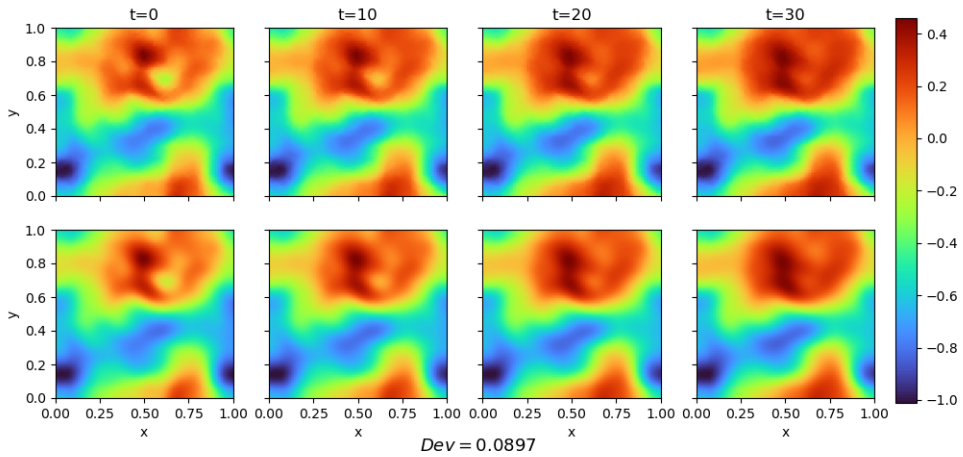


(a) Representation states at the beginning of FNO layers in two trials of Epoch 0

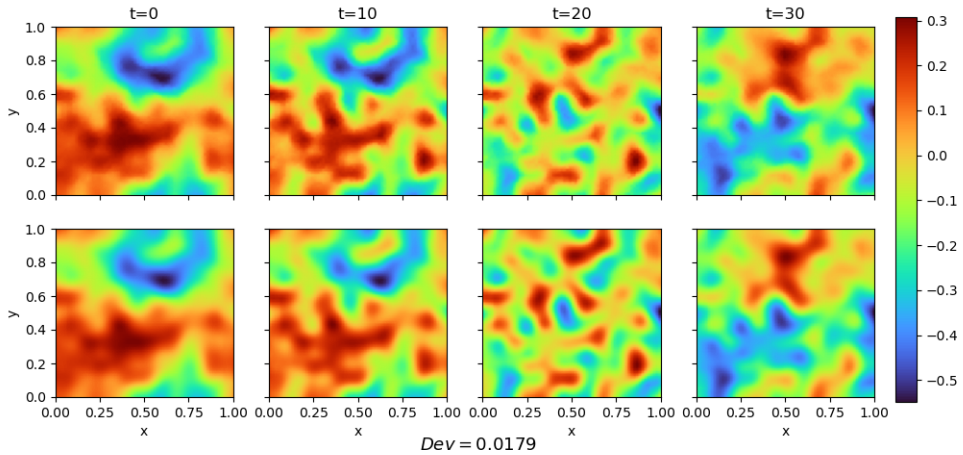


(b) Representation states at the beginning of FNO layers in two trials of Epoch 500

Figure C1: Visualization on different representation states at the beginning of FNO layers.

As a result, we present the one-v.s.-all differences of different epochs in the training process, to validate the convergence, as shown in Figure. C3.

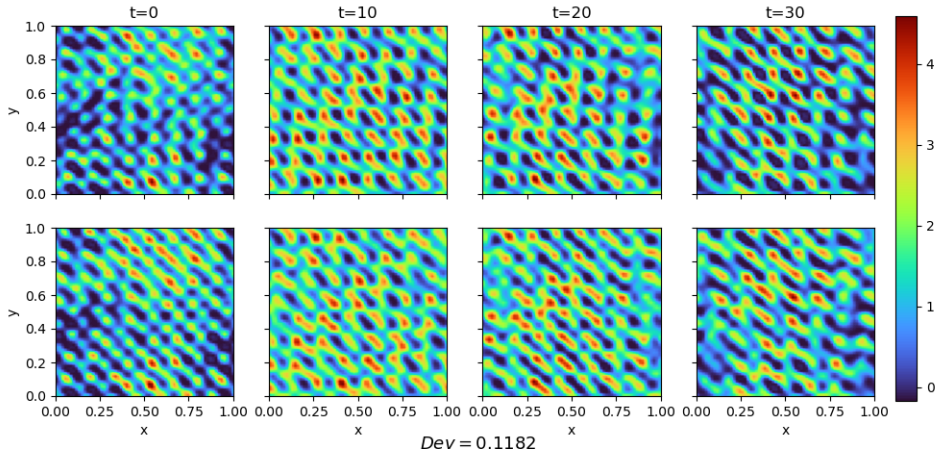


(a) Representation states in the end of FNO layers in two trials of Epoch 0

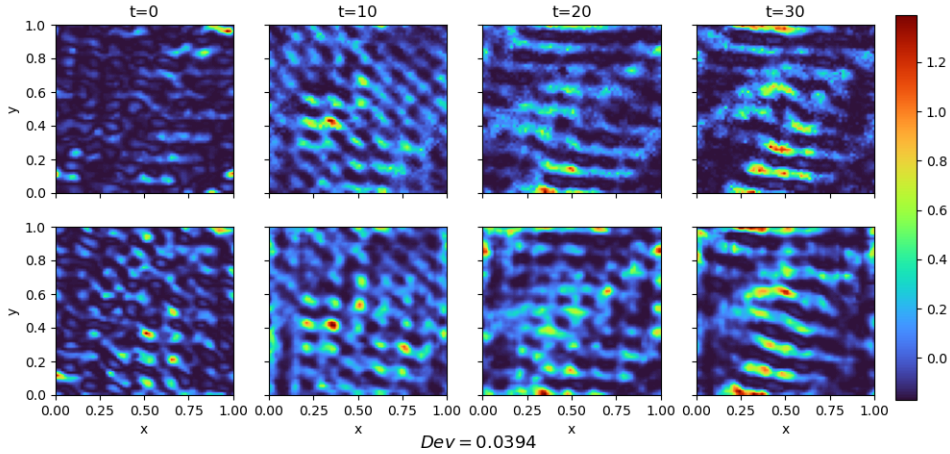


(b) Representation states in the end of FNO layers in two trials of Epoch 500

Figure C2: Visualization on different representation states in the end of FNO layers.

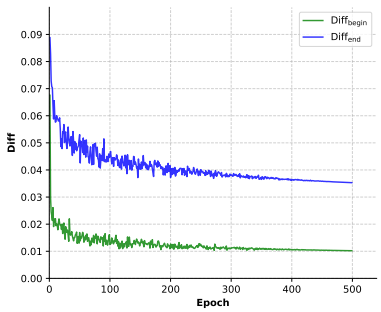


Figure C3: Convergence of Diff.